A Cu-Based Near-IR Active MOF with an Ion-Pair Guest Exhibiting Versatile and Selective Gas-Solid Reactivity

Rajat Saha,[a,*] Alejandro Cortés-Villena,[b] Silvia Gómez-Coca,[c] Alberto Fernández-Alarcón,[b] Joaquín Calbo,[b] Raquel E. Galian,[b] Enrique Ortí,[b] Eliseo Ruiz,[c] Mónica Giménez-Marqués,[b] Samia Benmansour,[a,*] and Carlos J. Gómez-García[a,*]

Dr. Rajat Saha, Prof. Samia Benmansour and Prof. Carlos J. Gómez-García

Departamento de Química Inorgánica, Universidad de Valencia, C/ Dr. Moliner, 50, 46100 Burjasot (Valencia), Spain. carlos.gomez@uv.es *(CJGG),* sam.ben@uv. *(SB) and* rajat.saha@uv.es *(RS).*

Dr. Alejandro Cortés-Villena, Dr. Alberto Fernández-Alarcón, Dr. Joaquín Calbo, Prof. Raquel E. Galian, Prof. Enrique Ortí and Prof. Mónica Giménez-Marqués

Institute of Molecular Science, University of Valencia, C/Catedrático José Beltrán Martínez 2, 46980 (Paterna) Valencia, Spain.

Dr. Silvia Gómez-Coca, and Prof. Eliseo Ruiz

Departament de Química Inorgànica i Orgànica and Institut de Recerca de Química Teòrica i Computacional, Universitat de Barcelona, Diagonal 645, 08028 Barcelona, Spain.

General, physical and chemical characterization:

All the chemicals were of analytical grade and used without further purification. Elemental analyses (carbon, hydrogen, oxygen and nitrogen) were performed using a Perkin-Elmer 240C elemental analyzer. Inductively coupled plasma-atomic emission spectroscopy (ICP-AES) analyses were performed with an Agilent 7900 ICP-MS spectrometer at the Microanalytical Service of the University of Valencia. IR spectroscopy was measured on a Nicolet Impact 410 spectrometer between 400 and 4000 cm^{-1}, using a KBr pellet.

The optical and photophysical characterization was performed on powder samples. Absorption spectra were recorded on a UV/Vis/NIR Perkin Elmer Lambda 1050 spectrophotometer in diffuse reflectance mode. The photoluminescence (PL) spectrum was recorded on a FLS1000 photoluminescence spectrometer (Edinburgh Instruments) equipped with a 450 W ozone free continuous xenon arc lamp and a photomultiplier (PMT-980) detector. A 980 nm continuous-wave (CW) laser excitation (2 W) was used for the NIR emission (NIR PMT, Hamamatsu Photonics). Time-resolved PL measurements were performed using the time-correlated single photon counting (TCSPC) technique. Pulsed-laser excitation employing a supercontinuum white NKT laser at indicated excitations under fixed repetition rates (7.8 MHz). Elemental mapping has also been carried out by the associated AzTec INCA software. The thermal analysis was carried out using a Mettler Toledo TG-DTA 85 thermal analyzer under a flow of N_2 (30 mL min^{-1}). The sample was heated at a rate of 10 ºC min^{-1} with inert alumina as a reference. The powder X-ray diffraction (PXRD) data were collected using Empyrean PANalytical powder diffractometer with CuKα radiation (λ = 1.54056 Å). Field Emission Scanning Electron Microscopy (FESEM) images were collected by using the Field Emission Scanning Electron microscope SCIOS 2 FIB-SEM and the corresponding EDX microanalysis was done by Oxford Ultim Max 170 Detector. X-band EPR spectra were collected with a Bruker ELEXSYS 580 equipped with a helium cryostat for polycrystalline samples of compounds **2** and **3** at 4 K and 300 K. High-energy resolution X-ray photoelectron spectroscopy (HR-XPS) measurements were performed in a SPECS GmbH system (base pressure 1.0×10^{-10} mbar) equipped with a PHOIBOS 150 2DCMOS hemispherical analyzer. Photoelectrons were excited with the Al-Kα line (1486.7 eV) of a monochromatic X-ray source µ-FOCUS 500 (SPECS GmbH). Measurements were taken at room temperature with a pass energy of 20 eV. For all of the HR-XPS measurements, freshly

exfoliated or degraded 2DPVKs were exposed to air and placed in ultrahigh vacuum (UHV) conditions.

Crystallographic Data Collection and Refinement

For all four compounds, the general methodology involved mounting a crystal on a Mylar loop (see dimensions in **Table S1**), coating it with Paratone oil, and collecting data using an XtaLAB Synergy R, DW system, HyPix diffractometer at approximately 120 K (119.99 K or 120.00 K). Data were measured using ω scans with Cu K_α radiation.

CrysAlisPro software (versions 1.171.42.49 and 1.171.43.60a)[1] was consistently used for: Indexing the diffraction pattern, determining the total number of runs and images, refining the unit cell, performing data reduction, scaling and absorption corrections (including multi-scan absorption correction using spherical harmonics implemented in the SCALE3 ABSPACK algorithm).

The structures were solved using the SHELXT 2018/2 program[2] (dual methods) using iterative methods and Olex2 1.5 as the graphical interface.[3] and refined by full matrix least squares minimization on F^2 using SHELXL 2018/3.[2] In all cases, non-hydrogen atoms were refined anisotropically and hydrogen atom positions were calculated geometrically and refined using the riding model.

A summary of the data collection and structure refinement is given in **Table S1**.

Table S1. Crystal data and refinement parameters for compounds **3**, **4-NH$_3$**, **5-HCl**, and **6-For**.

Compound	**3**	**4-NH$_3$**	**5-HCl**	**6-For**
Formula	$C_{24}H_{16}Cl_4Cu_5N_4O_9$	$C_6H_4CuNO_4$	$C_{12}H_{16}Cl_6Cu_2N_2O_6$	$C_5H_{11}CuNO_6$
CCDC	2455053	2455054	2455055	2455056
$D_{calc.}$ (g cm^{-3})	1.524	2.012	2.006	1.885
μ (mm^{-1})	5.512	4.120	9.998	3.677
Formula Weight	963.91	217.64	624.05	244.69
Color	green	blue	green	green
Shape	cube-shaped	cube-shaped	block-shaped	block-shaped
Size (mm^3)	0.04×0.03×0.03	0.05×0.05×0.04	0.14×0.12×0.10	0.07×0.06×0.04
T (K)	120.00(10)	120.00(10)	119.99(10)	119.99(10)
Crystal System	orthorhombic	monoclinic	triclinic	monoclinic
Flack Parameter	0.008(13)	-	-	-
Space Group	*I*222	*P*2$_1$/*n*	*P*-1	*I*2/*a*
a (Å)	13.9827(3)	3.5276(2)	7.94410(10)	11.3902(11)
b (Å)	12.9083(4)	15.7899(8)	8.6447(2)	8.6593(11)
c (Å)	11.6404(4)	12.9885(7)	8.6798(2)	8.7845(9)
α (º)	90	90	116.447(2)	90
β (º)	90	96.733(5)	98.670(2)	95.785(10)
γ (º)	90	90	96.527(2)	90
V (Å^3)	2101.01(11)	718.48(7)	516.47(2)	862.01(16)
Z	2	4	1	4
Wavelength (Å)	1.54184	1.54184	1.54184	1.54184
Radiation type	Cu K$_a$	Cu K$_a$	Cu K$_a$	Cu K$_a$
Θ_{min} (º)	4.662	4.426	5.755	6.433
Θ_{max} (º)	66.655	76.221	66.661	66.574
Measured Refl's.	5138	7540	8572	3380
Indep't Refl's	1873	1477	1825	751
Refl's I ≥ 2 σ(I)	1818	1394	1794	557
R_{int}	0.0248	0.0354	0.0238	0.1214
Parameters	107	122	129	63
Restraints	0	12	5	9
Largest Peak	0.247	2.223	1.004	0.793
Deepest Hole	-0.453	-0.608	-0.429	-0.930
GooF	1.220	1.250	1.185	1.020
wR_2 (all data)	0.0721	0.1768	0.0794	0.1360
wR_2	0.0719	0.1753	0.0747	0.1225
R_1 (all data)	0.0256	0.0609	0.0292	0.0851
R_1	0.0248	0.0583	0.0280	0.0547

Table S2. Main bond distances (Å) for compound $(Me_2NH_2)(Cu^ICl_2)$@$[Cu_4(INA)_4Cl_2O]\cdot 1.5dmf$ (**3**).

Atom	Atom	Distance (Å)	Atom	Atom	Distance (Å)
Cu1	Cl1	2.3543(13)	O11	C1	1.238(5)
Cu1	O2	1.9086(6)	N1	C5	1.359(6)
Cu1	O1	1.969(3)	N1	C4	1.351(6)
Cu1	O11[1]	2.304(3)	C5	C6	1.370(7)
Cu1	N1[2]	1.982(4)	C3	C2	1.388(6)
Cu10	Cl10	2.101(3)	C3	C4	1.370(7)
Cu10	Cl10[3]	2.101(3)	C1	C2	1.526(6)
O1	C1	1.254(6)	C6	C2	1.391(7)

(1) 1 - x, 1 - y, z; (2) 3/2 - x, -1/2 + y, 3/2 - z; (3) 2 - x, +y, 1 - z.

Table S3. Main bond angles (º) for compound $(Me_2NH_2)(Cu^ICl_2)$@$[Cu_4(INA)_4Cl_2O]\cdot 1.5dmf$ (**3**).

Atom	Atom	Atom	Angle (º)	Atom	Atom	Atom	Angle (º)
O2	Cu1	Cl1	86.06(3)	Cu1	O2	Cu1[4]	106.72(3)
O2	Cu1	O1	90.86(10)	C1	O1	Cu1	120.6(3)
O2	Cu1	O11[1]	96.10(8)	C1	O11	Cu1[1]	116.0(3)
O2	Cu1	N1[2]	168.87(12)	C5	N1	Cu1[6]	120.0(3)
O1	Cu1	Cl1	167.80(11)	C4	N1	Cu1[6]	121.6(3)
O1	Cu1	O11[1]	106.81(14)	C4	N1	C5	118.2(4)
O1	Cu1	N1[2]	89.30(15)	N1	C5	C6	122.0(5)
O11[1]	Cu1	Cl1	85.27(9)	C4	C3	C2	120.0(4)
N1[2]	Cu1	Cl1	91.47(12)	O1	C1	C2	114.5(4)
N1[2]	Cu1	O11[1]	94.51(14)	O11	C1	O1	128.3(4)
Cl10[3]	Cu10	Cl10	180.0	O11	C1	C2	117.2(4)
Cu1	Cl1	Cu1[4]	81.16(6)	C5	C6	C2	119.8(4)
Cu1[1]	O2	Cu1[5]	106.72(3)	C3	C2	C1	120.9(4)
Cu1[4]	O2	Cu1[5]	109.70(4)	C3	C2	C6	117.9(4)
Cu1	O2	Cu1[1]	109.70(4)	C6	C2	C1	121.2(4)
Cu1	O2	Cu1[5]	112.04(3)	N1	C4	C3	122.0(4)
Cu1[4]	O2	Cu1[1]	112.04(3)				

(1) 1 - x, 1 - y, z; (2) 3/2 - x, -1/2 + y, 3/2 - z; (3) 2 - x, +y, 1 - z; (4) 1 - x, y, 1 - z; (5) x, 1 - y, 1 - z; (6) 3/2 -x, ½ + y, 3/2 - z.

Table S4. Main bond distances (Å) for compound [Cu(INA)(OH)]·H_2O (**4-NH_3**).

Atom	Atom	Distance (Å)	Atom	Atom	Distance (Å)
$Cu1^1$	Cu1	2.9705(13)	N1	C5	1.357(6)
$Cu1^2$	O1	2.256(3)	N1	C1	1.343(6)
Cu1	O1	1.939(3)	C5	C4	1.379(7)
$Cu1^3$	O1	1.974(3)	C6	C3	1.515(6)
$Cu1^4$	O6B	2.006(3)	C4	C3	1.389(7)
Cu1	N1	1.989(4)	C1	C2	1.381(7)
O6B	C6	1.266(6)	C3	C2	1.394(7)
O6A	C6	1.246(6)			

(1) 1 - x, -y, 1 - z; (2) 2 - x, -y, 1 - z; (3) 1 - x, -y, 1 - z; (4) x + ½, -y + ½, z - ½.

Table S5. Main bond angles (º) for compound [Cu(INA)(OH)]·H_2O (**4-NH_3**).

Atom	Atom	Atom	Angle (º)	Atom	Atom	Atom	Angle (º)
O1	$Cu1^1$	Cu1	41.05(9)	Cu1	$O1^2$	Cu1	94.71(13)
$O1^1$	$Cu1^1$	Cu1	40.18(9)	$Cu1^1$	$O1^2$	Cu1	112.84(14)
$O1^2$	$Cu1^1$	Cu1	101.79(8)	C6	$O6B^4$	Cu1	126.2(3)
O1	$Cu1^1$	O1	81.23(13)	C5	N1	Cu1	117.0(3)
O1	$Cu1^2$	O1	85.29(13)	C1	N1	Cu1	123.2(3)
$O1^1$	$Cu1^2$	O1	112.85(14)	C1	N1	C5	118.3(4)
O1	$Cu1^3$	O6B	95.21(13)	N1	C5	C4	122.0(4)
$O1^1$	$Cu1^3$	O6B	154.93(14)	O6B	C6	C3	115.2(4)
O1	Cu1	N1	172.00(15)	O6A	C6	O6B	126.9(4)
$O1^1$	Cu1	N1	90.95(14)	O6A	C6	C3	117.9(4)
$O6B^3$	$Cu1^1$	Cu1	131.39(10)	C5	C4	C3	119.7(4)
$O6B^3$	$Cu1^2$	O1	91.43(13)	N1	C1	C2	122.5(4)
N1	$Cu1^1$	Cu1	131.12(12)	C4	C3	C6	121.1(4)
N1	$Cu1^2$	O1	96.26(14)	C4	C3	C2	118.1(4)
N1	$Cu1^3$	O6B	92.60(15)	C2	C3	C6	120.8(4)
Cu1	$O1^1$	Cu1	98.77(13)	C1	C2	C3	119.4(5)

(1) 1 - x, -y, 1 - z; (2) 2 - x, -y, 1 - z; (3) x + ½, -y + ½, z - ½; (4) x - ½, -y + ½, z + ½

Table S6. Main bond distances (Å) for compound $(HINA)_2[Cu_2Cl_6(H_2O)_2]$ (**5-HCl**).

Atom	Atom	Distance (Å)	Atom	Atom	Distance (Å)
Cu1	Cl1	2.2852(6)	N1	C5	1.345(3)
Cu1	Cl2	2.2515(6)	N1	C4	1.335(3)
Cu1	Cl3	2.2711(6)	C1	C2	1.498(3)
Cu1	O1W	1.9725(17)	C3	C2	1.395(3)
Cu1	$Cl2^1$	2.856(6)	C3	C4	1.375(4)
O1	C1	1.225(3)	C2	C6	1.391(4)
O11	C1	1.3079(10)	C5	C6	1.371(4)

(1) -x, -y, -z

Table S7. Main bond angles (º) for compound $(HINA)_2[Cu_2Cl_6(H_2O)_2]$ (**5-HCl**).

Atom	Atom	Atom	Angle (º)	Atom	Atom	Atom	Angle (º)
Cl2	Cu1	Cl1	92.45(2)	O11	C1	C2	114.60(19)
Cl2	Cu1	Cl3	93.09(2)	C4	C3	C2	118.6(2)
Cl3	Cu1	Cl1	157.48(3)	C3	C2	C1	121.2(2)
O1W	Cu1	Cl1	89.65(5)	C6	C2	C1	118.7(2)
O1W	Cu1	Cl2	172.86(6)	C6	C2	C3	120.1(2)
O1W	Cu1	Cl3	87.53(5)	N1	C5	C6	119.3(2)
C4	N1	C5	123.3(2)	C5	C6	C2	119.0(2)
O1	C1	O11	125.7(2)	N1	C4	C3	119.7(2)
O1	C1	C2	119.67(17)				

Table S8. Main bond distances (Å) for compound $(Me_2NH_2)[Cu(HCOO)_3]$ (**6-For**).

Atom	Atom	Distance (Å)	Atom	Atom	Distance (Å)
Cu1	O1	1.967(4)	O1	C1	1.256(5)
Cu1[1]	O1	1.967(4)	O3	C2	1.266(6)
Cu1[1]	O2	1.970(4)	O2	C2	1.247(7)
Cu1	O2	1.970(4)	N100	C100	1.484(7)
Cu1[1]	O3	2.452(5)	N100[2]	C100	1.484(7)

(1) -x, 1 - y, 1 - z; (2) -x + 3/2, y, 2 - z.

Table S9. Main bond angles (º) for compound $(Me_2NH_2)[Cu(HCOO)_3]$ (**6-For**).

Atom	Atom	Atom	Angle (º)	Atom	Atom	Atom	Angle (º)
O1	Cu1[1]	O1	180.0	C1	O1	Cu1	124.1(4)
O1[1]	Cu1	O2	88.52(15)	C2	O2	Cu1	125.4(3)
O1	Cu1	O2	91.48(15)	C100	N100[2]	C100	111.9(7)
O1	Cu1[1]	O2	88.52(15)	O1[3]	C1	O1	124.4(7)
O1[1]	Cu1[1]	O2	91.48(15)	O2	C2	O3	123.9(5)
O2[1]	Cu1	O2	180.0				

(1) -x, 1 - y, 1 - z; (2) -x + 3/2, y, 2 - z; (3) -x+1/2, y, 1-z

Bond Valence Sum (BVS) Calculations

The BVS calculations performed for compounds **3**, **4-NH$_3$**, **5-HCl**, and **6-For** show that the oxidation state of the Cu ions is in all cases +2 except in the inserted $CuCl_2^-$ anion (Cu10) where it is, as expected, +1 (**Table S10**).

Table S10. BVS calculations for the Cu ions in compounds **3**, **4-NH$_3$**, **5-HCl**, and **6-For**.

Compound	Cu center	Valence sum[a]	Valence sum[b]	Valence sum[c]
3	Cu1	1.527	**2.072**	2.407
	Cu10	**1.037**	1.522	1.878
4-NH$_3$	Cu1	1.416	**1.867**	2.144
5-HCl	Cu1	1.363	**1.892**	2.317
6-For	Cu1	1.581	**1.790**	2.129

(a) assuming a valence of +1; (b) assuming a valence of +2; (c) assuming a valence of +3.

Methods

Magnetic measurements. Variable temperature susceptibility measurements were carried out in the temperature range 2-300 K with an applied magnetic field of 0.1 T, on polycrystalline samples of compounds **2**, **3**, **5-HCl**, and **6-For** (with masses of 14.094, 10.566, 12.674 and 15.187 mg, respectively) using a Quantum Design MPMS-XL-7 SQUID magnetometer. The susceptibility data were corrected for the sample holders previously measured using the same conditions and for the diamagnetic contributions of the compounds as deduced by using Pascal´s constant tables.[4]

Gas Adsorption Study: N_2 volumetric isotherm was measured using a Tristar II apparatus (Micromeritics) at -196 °C (77 K). Before the analysis, the sample was degassed at 120 °C (393 K) under vacuum overnight. High-pressure adsorption CO_2 isotherm was measured at 298 K in an IGA-100 gravimetric gas sorption analyzer (Hiden Isochema) using approximately 20 mg of sample. Before the adsorption experiment, the sample was outgassed at 120 °C (393 K) under vacuum (10^{-5} Pa) for two hours. Equilibrium conditions corresponded to a 600 s interval and 0.001 mg min^{-1} tolerance.

Synthesis of compound [Cu(INA)$_2$]·dmf (2). Compound **2** was prepared starting from the monomer $[Cu(INA)_2(H_2O)_4]$ (**1**), synthesized as described in the literature,[5] and characterized by single crystal X-ray diffraction (SCXRD) analyses. The precursor $[Cu(INA)_2(H_2O)_4]$ (**1**) (0.2 mmol) and $CuCl_2$ (0.2 mmol) were mixed in a mixture of 4 mL of water with 1 mL of dmf and the mixture was treated solvothermally at 105 ºC in a closed 10 mL vial. After 24 h, deep-blue colored cube-like crystals of compound **2** were obtained. The crystals were collected and characterized by SCXRD.

Synthesis of compound (Me$_2$NH$_2$)(Cu^{I}Cl$_2$)@[Cu$_4$(INA)$_4$Cl$_2$O]·1.5dmf (3). Continuation of the previously described reaction for 24 h more, leads to the formation of green cubes of compound **3**. These green single crystals were collected and characterized by SC-XRD, powder X-ray diffraction (PXRD) and thermal analysis. Elemental analysis (%) for $C_{30.5}H_{34.5}Cu_5N_{6.5}O_{10.5}Cl_4$ (MW = 1119.675): Calc. (Found). C, 32.69 (31.82); H, 3.11 (3.06); N, 8.13 (7.89); O, 15.00 (15.35); Cu, 28.4 (27.7).

Single-crystal-to-single-crystal (SC-SC) transformation of compound 3 into 4-NH_3 in NH_3 vapor. A few green crystals of **3** were placed in contact with NH_3 vapor in a closed container. The evolution of the crystals was monitored by naked eye color change. The crystals transform from green to turquoise-blue with the formation of a white residue. Turquoise-blue single crystals were separated and characterized by single crystal X-ray diffraction (SCXRD) analysis.

Dissolution recrystallisation structural transformation (DRST) of compound 3 into 5-HCl in HCl vapor. A few green crystals of **3** were placed in contact with aqueous HCl vapor in a closed container. The evolution of the crystals was monitored by naked eye color change. Within a couple of minutes, the green crystals become brown and redissolve in a droplet formed around them and crystallize from the droplet lime-green plate-like crystals. The crystals were separated and characterized by SCXRD analysis.

DRST of compound 3 into 6-For in HCOOH vapor. A few green crystals of **3** were placed in contact with formic acid vapors in a closed container. The evolution of the crystals was monitored by naked eye color change. The crystals dissolved in a droplet formed around them and crystallize from the droplet as sea-green single crystals after a few minutes. The crystals were separated and characterized by SCXRD analysis.

DRST of compound 3 into 7-Ac in CH_3COOH vapor. A few green crystals of **3** were placed in contact with acetic acid vapors in a closed container. The evolution of the crystals was monitored by naked eye color change. The crystals dissolved in a droplet formed around them and crystallize from the droplet as dark-green single crystals after a few minutes. The crystals were separated and characterized by SCXRD analysis, that showed that they correspond to the well-known $[Cu_2(CH_3COO)_4(H_2O)]$ dimer.[6]

Inertness of 3. Compound **3** shows a remarkable stability, for at least seven days over a wide range of chemicals, including H_2O, methanol, ethanol, acetone, pyridine, H_2SO_4, H_3PO_4, and Et_3N.

Statistical Analysis. The data of the thermogravimetric analysis are represented as provided by the thermal analyzer without any correction or transformation. The magnetic measurements data are corrected for the sample holders previously measured using the same conditions and for the diamagnetic contributions of the compounds, as indicated in the experimental section.

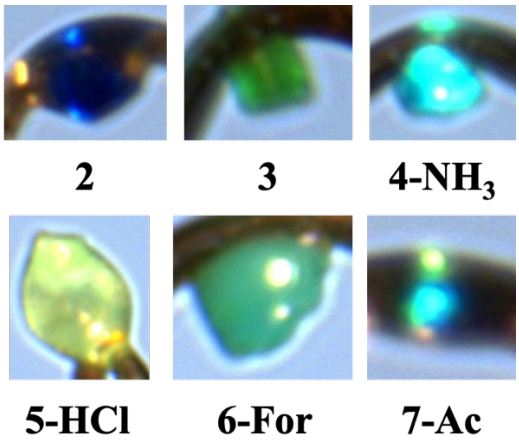

Figure S1. Images of the different crystals mounted in the mylar loops: deep blue crystals of MOF **2**, green cubic crystals of MOF **3**, turquoise blue crystals of **4-NH$_3$**, lime green crystals of **5-HCl**, sea green crystals of **6-For** and green crystals of **7-Ac**.

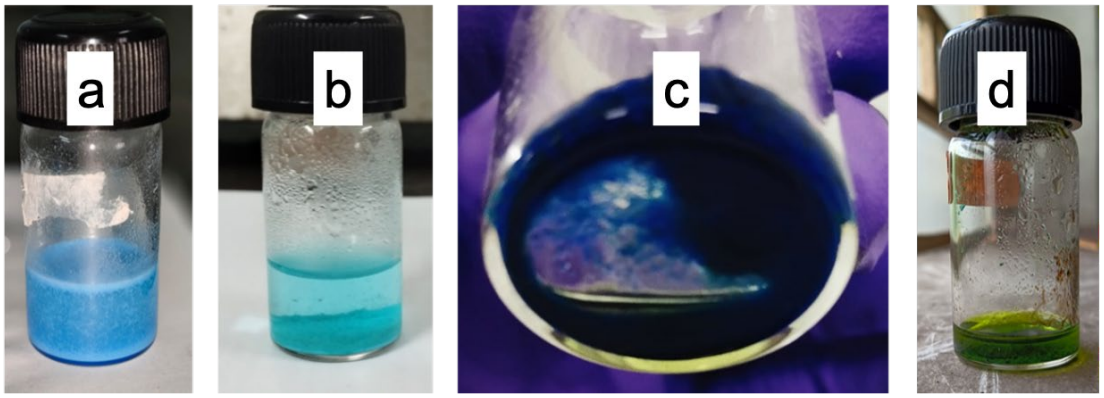

Figure S2. Solution-phase structural transformation of **1** into **2** and **3** during the reaction of **1** with $CuCl_2$ in a water/dmf (4/1) mixture. (**a**) The initial reaction mixture of **1** with $CuCl_2$ in dmf and water before the reaction. (**b**) After 2 h of heating the reaction mixture. (**c**) The formation of blue cubes of MOF **2**. (**d**) The formation of green cubes of **3**.

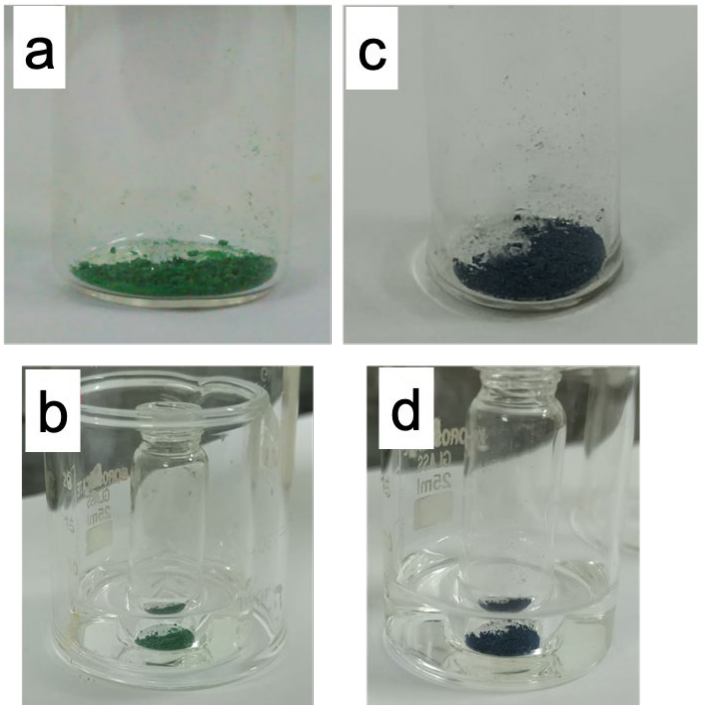

Figure S3. Structural transformation of MOF **3** in presence of NH_3 vapor. The color change as well as the change of morphology can be observed by naked eye. (**a**) and (**b**) Initial stage. (**c**) and (**d**) after exposure to NH_3 for 5 min.

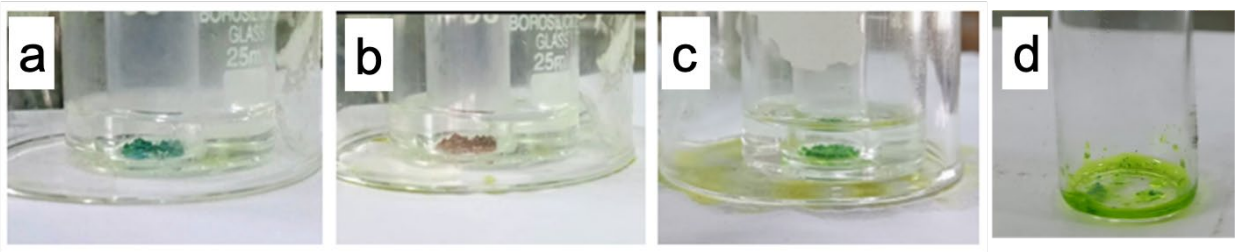

Figure S4. Structural transformation of MOF **3** in presence of HCl vapor. (**a**) Initial state. (**b**) Formation of the intermediate brown phase. (**c**) Formation of lime green color liquid phase. (**d**) Lime green colored plate-like single crystals formed from the liquid phase.

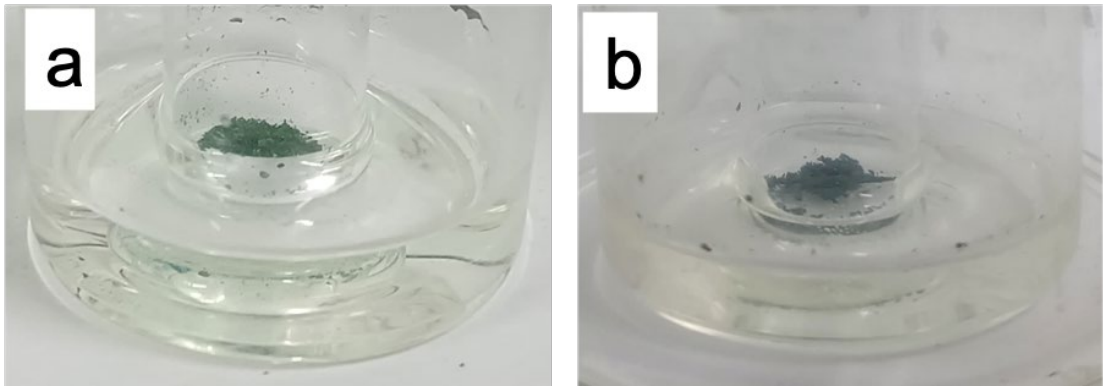

Figure S5. Structural transformation of MOF **3** in presence of formic acid vapor: (**a**) Initial stage.

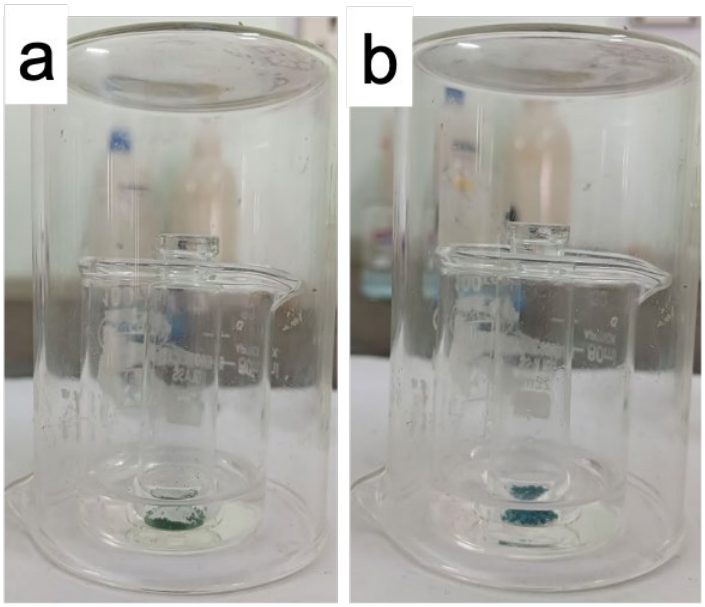

Figure S6. Structural transformation of MOF **3** in presence of acetic acid vapor: (**a**) Initial stage. (**b**) After 1 h.

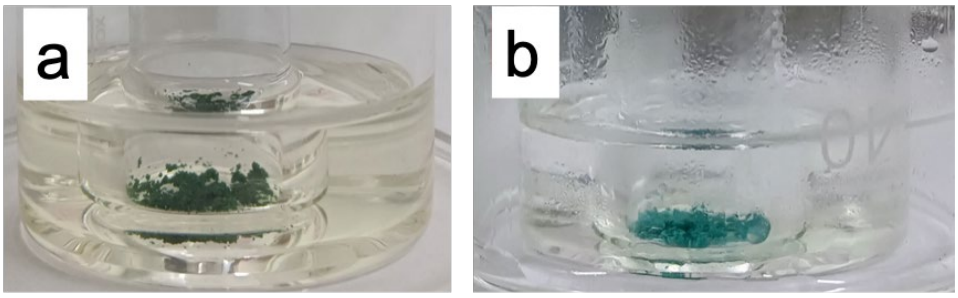

Figure S7. Transformation of MOF **3** in presence of HNO_3 vapor. (**a**) Initial stage. (**b**) After 24 h.

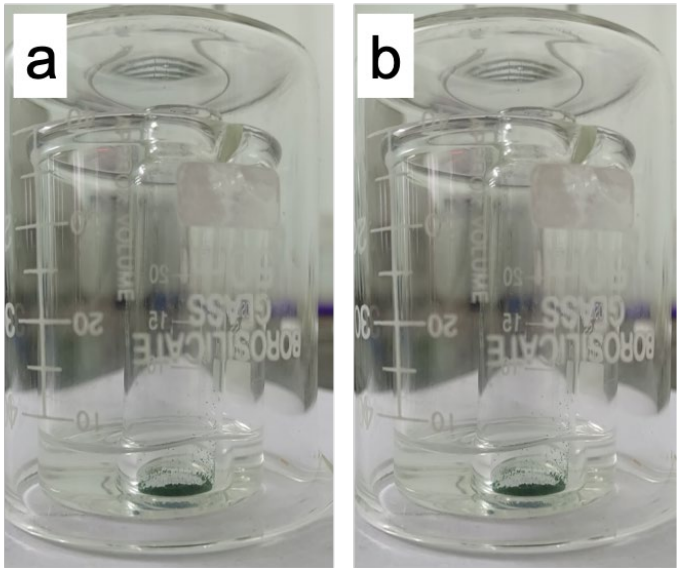

Figure S8. Stability of MOF **3** in presence of $(CH_3CH_2)_3N$ vapor. (**a**) Initial stage. (**b**) After 24 h.

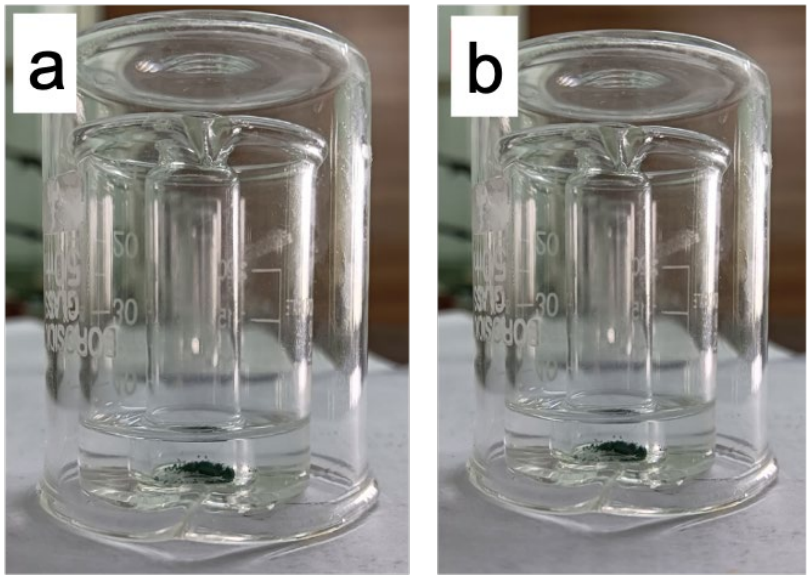

Figure S9. Stability of MOF **3** in presence of H_2SO_4 vapor: (**a**) Initial stage. (**b**) After 7 days.

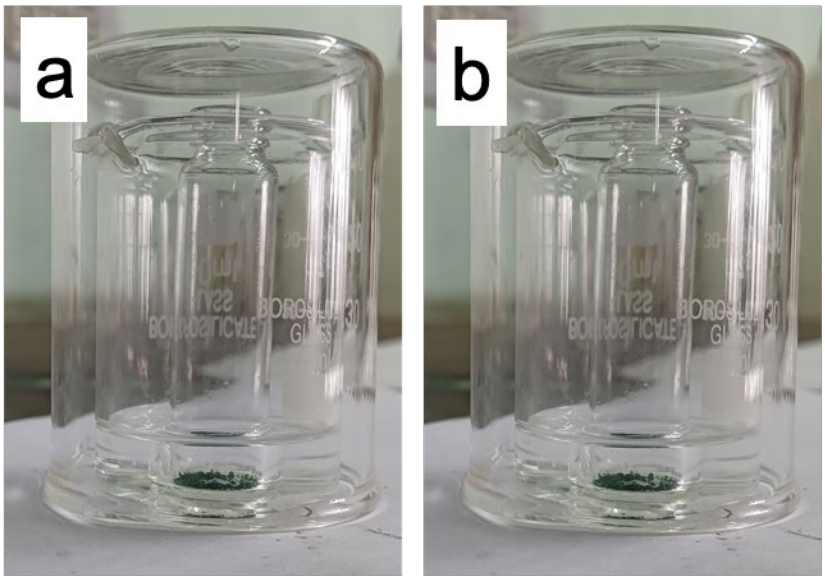

Figure S10. Stability of MOF **3** in presence of H_3PO_4 vapor: (**a**) Initial stage. (**b**) After 7 days.

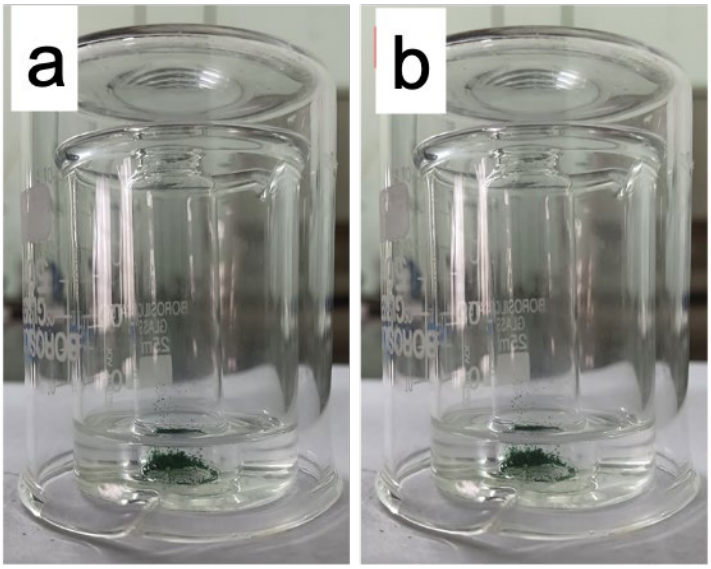

Figure S11. Stability of MOF **3** in presence of methanol vapor: (**a**) Initial stage. (**b**) After 7 days.

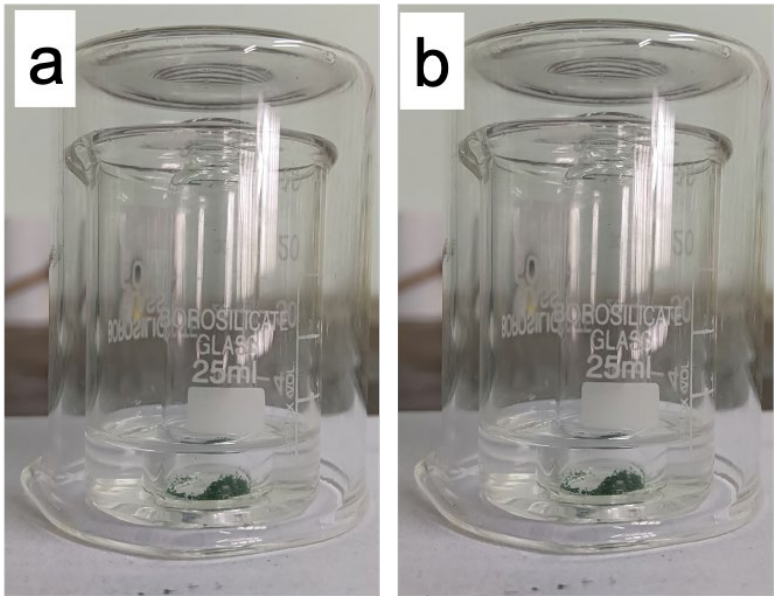

Figure S12. Stability of MOF **3** in presence of acetone vapor: (**a**) Initial stage. (**b**) After 7 days.

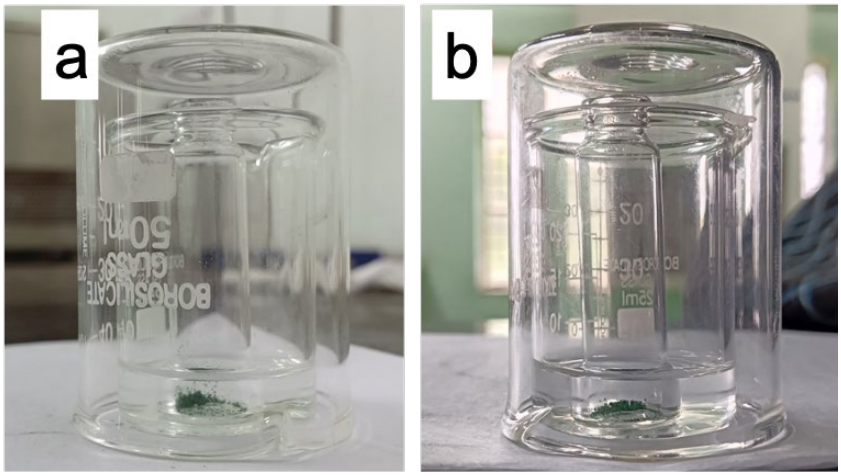

Figure S13. Stability of MOF **3** in presence of acetonitrile vapor: (**a**) Initial stage. (**b**) After 7 days.

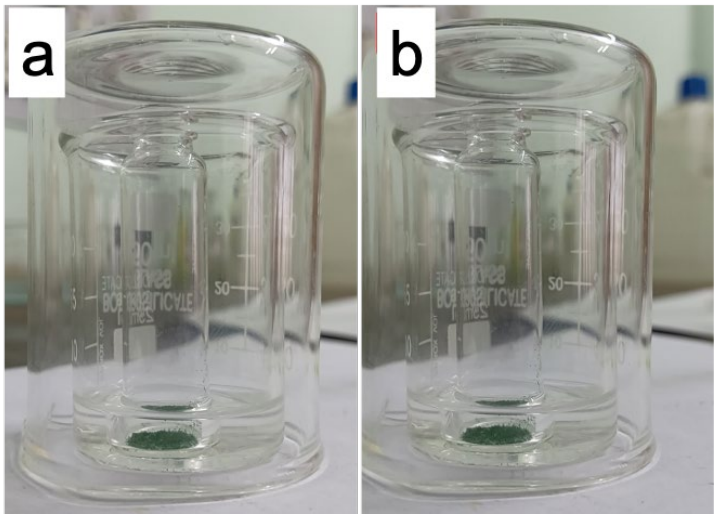

Figure S14. Stability of MOF **3** in presence of ethanol vapor: (**a**) Initial stage. (**b**) After 7 days.

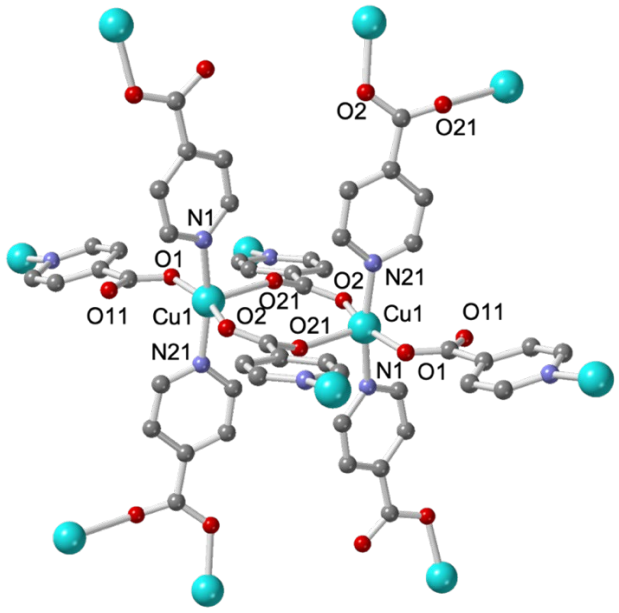

Figure S15. Fragment of the structure of MOF **2** showing the connectivity of the Cu^{II} dimers and the labelling scheme.

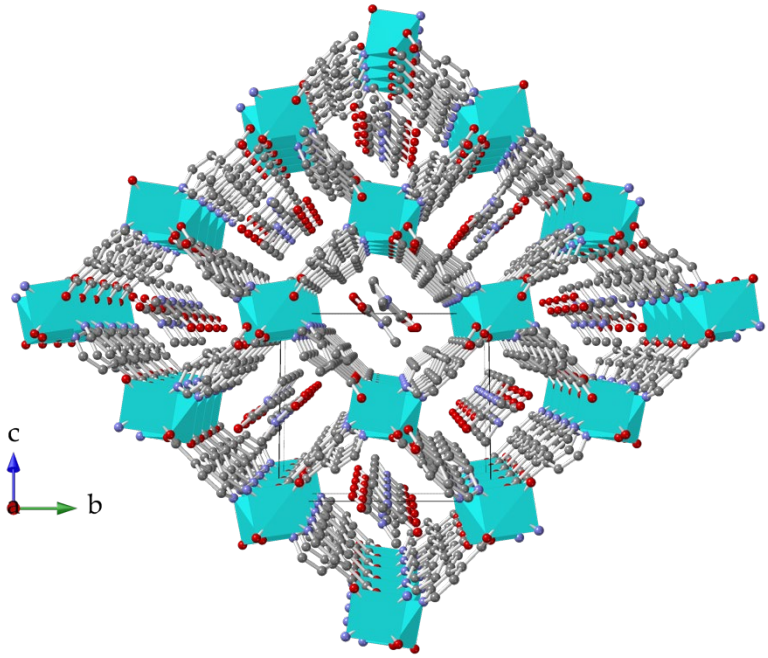

Figure S16. Perspective view of the 3D packing of MOF **2** showing the guest dmf molecules within the square channels along the *a* direction. Hydrogen atoms are omitted for clarity. Color code: C = grey, O = red, N = dark blue, and Cu = light blue.

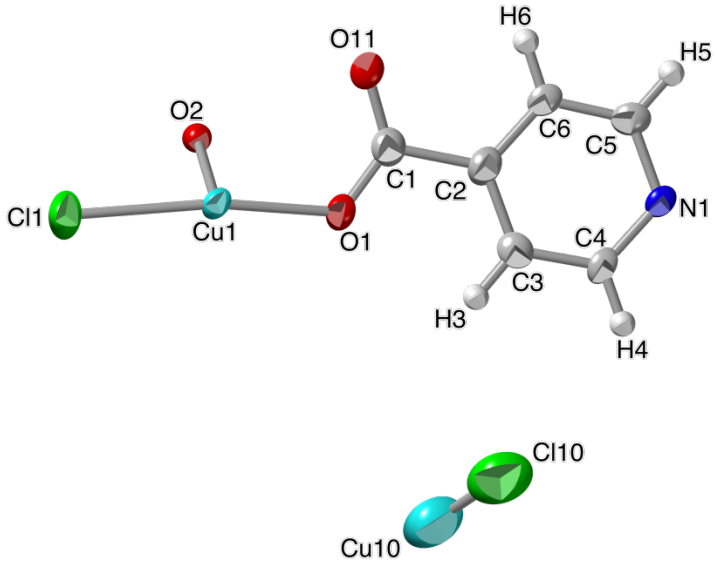

Figure S17. Asymmetric unit of MOF **3** showing the labelling scheme. Ellipsoids drawn at 80 % probability level.

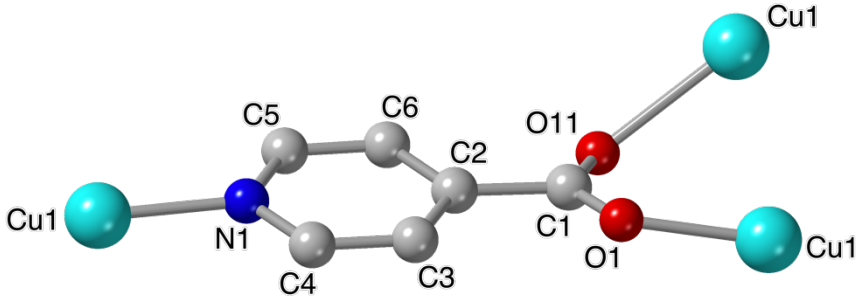

Figure S18. Connectivity of the INA^- ligand in MOF **3** with the labelling scheme.

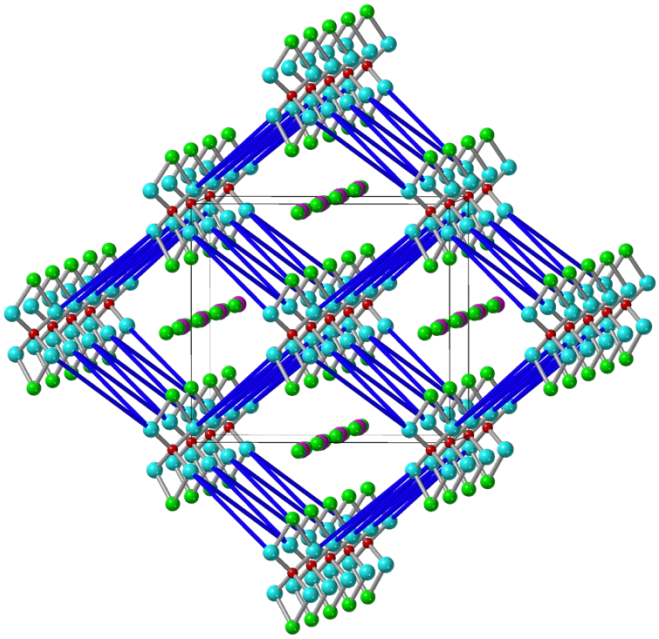

Figure S19. Schematic connectivity of the Cu_4O tetrahedra in MOF **3**. Dark blue lines represent the INA^- ligands connecting each Cu_4O tetrahedron with its eight neighbors. Color code: Cu^{II} = light blue, Cl = green, O = red, and Cu^{I} = pink.

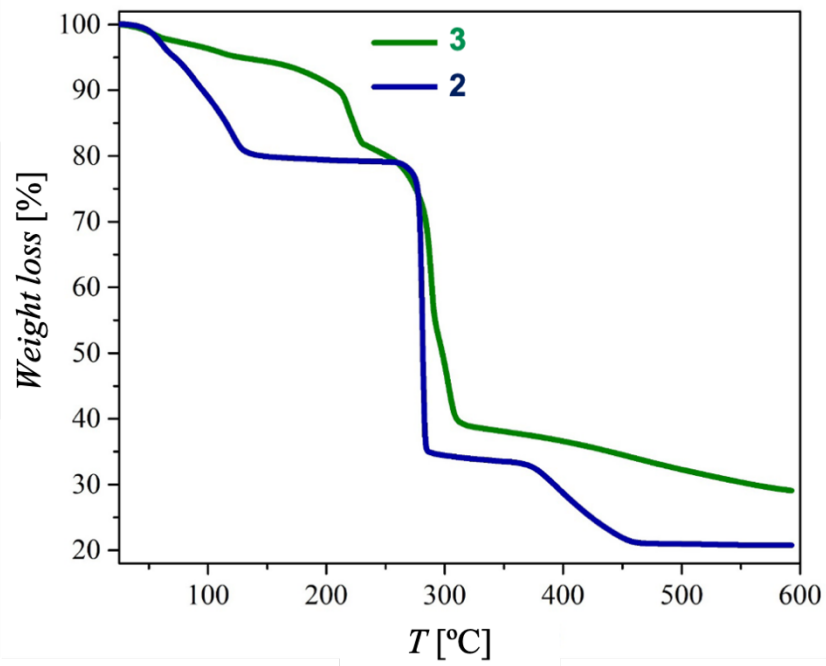

Figure S20. Thermogravimetric analysis of MOFs **2** and **3**.

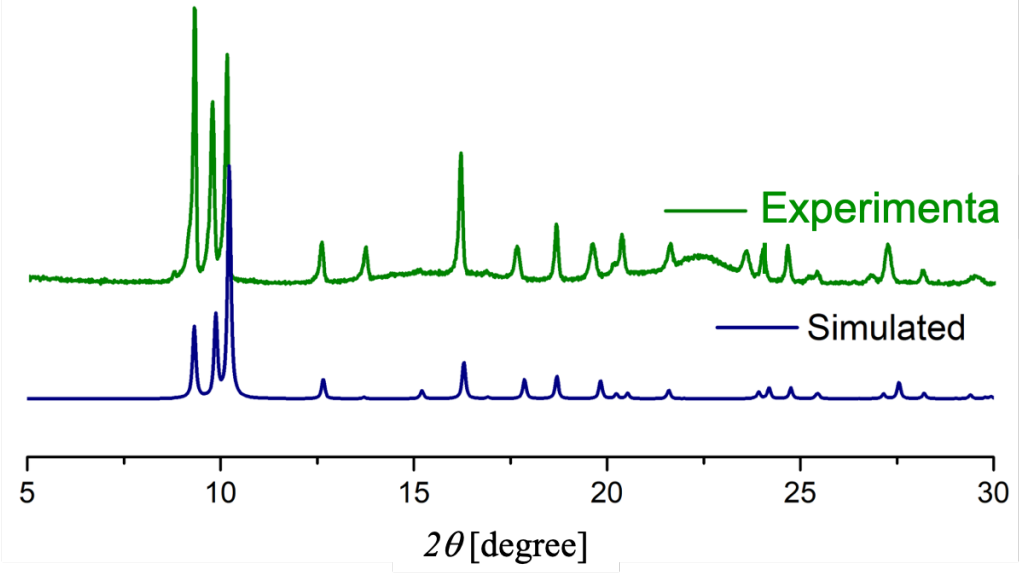

Figure S21. Experimental and simulated powder X-ray diffractograms for MOF **3**.

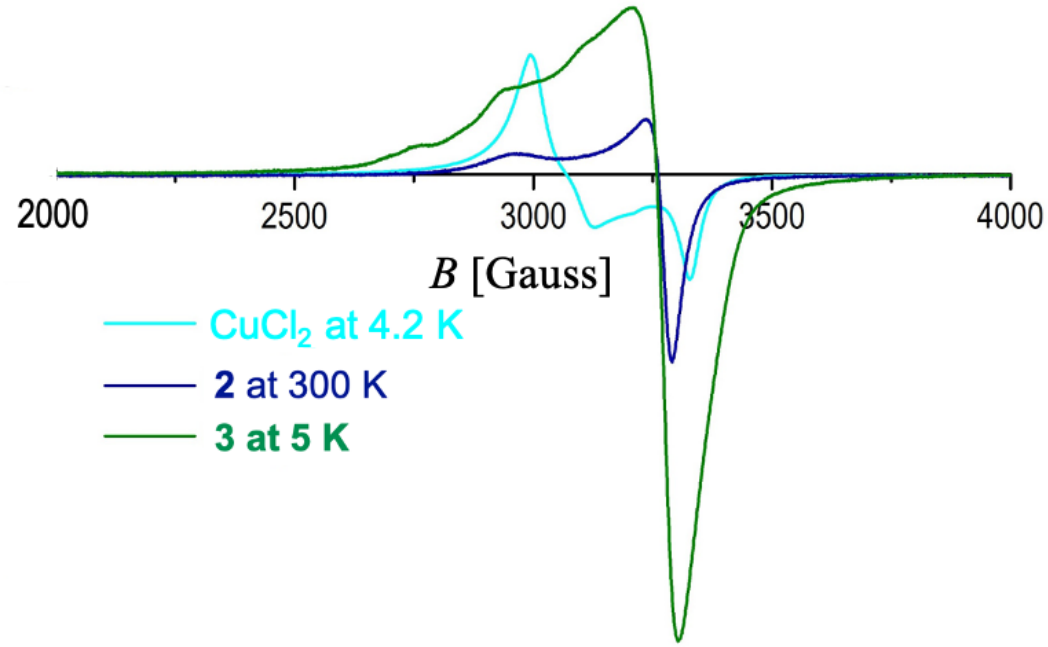

Figure S22. EPR spectra of $Cu^{II}Cl_2$ and of MOFs **2** and **3** at different temperatures.

Magnetic Properties of 2 and 3

The product of the magnetic susceptibility per Cu^{2+} dimer times the temperature ($\chi_m T$) for compound **2** shows a room temperature value of around 0.8 cm^3 K mol^{-1}, close to the expected value for two isolated S = ½ Cu^{2+} ions with g close to 2. When the temperature is decreased, $\chi_m T$ remains constant down to around 50 K and shows a progressive decrease at lower temperatures to reach a value of around 0.65 cm^3 K mol^{-1} at 2 K (Figure S23). This behavior indicates the presence of an antiferromagnetic coupling between the Cu^{2+} ions connected through the double carboxylate bridge. Accordingly, we have fitted the magnetic data to a simple Bleaney and Bowers S = ½ dimer model[7] with the parameters displayed in **Table S11**.

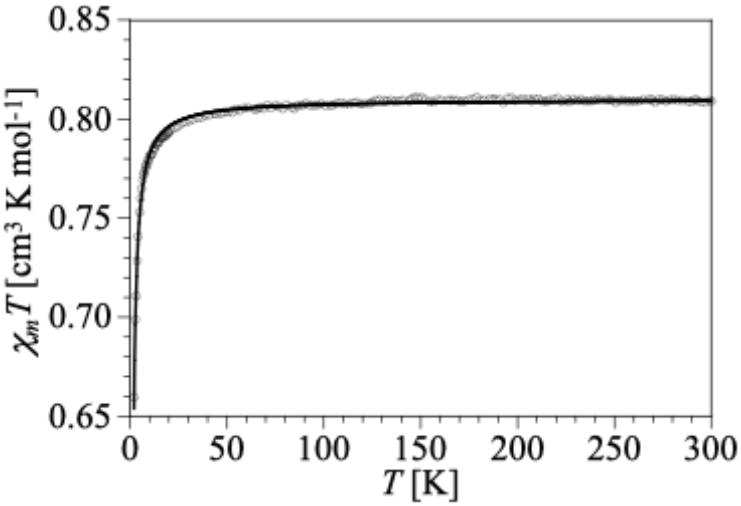

Figure S23. Thermal variation of the product of the magnetic susceptibility per Cu dimer times the temperature ($\chi_m T$) for compound **2**. Solid line is the best fit to a S = ½ dimer model.

In compound **3** the product of the magnetic susceptibility per Cu_4 tetramer times the temperature ($\chi_m T$) shows a room temperature value of around 1.5 cm^3 K mol^{-1}, close to the expected value for four isolated S = ½ Cu^{2+} ions with g close to 2. When the temperature is decreased, $\chi_m T$ shows a progressive decrease to reach a value of around 0.05 cm^3 K mol^{-1} at 2 K (Figure S24). This behavior indicates the presence of a predominant antiferromagnetic coupling between the Cu^{2+} ions connected through the single oxido bridge in the Cu_4O central cluster. As can be seen in the inset in Figure S24, the central Cu_4O cluster shows three different Cu···Cu exchange pathways: two Cu-O-Cu bridges with angles of 112.04º and 109.70º (J_1 and J_2,

respectively) and one (J_3) with a Cu-Cl-Cl bridge, besides the Cu-O-Cu one, with a Cu-O-Cu bond angle of 106.72º. Accordingly, we have fitted the magnetic data to a simple tetramer model with three different coupling constants using the program PHI[8] with the parameters displayed in **Table S11**. Note that, in order to reproduce the plateau at very low temperatures, we need to introduce a monomeric S = ½ paramagnetic impurity or around 4 %.

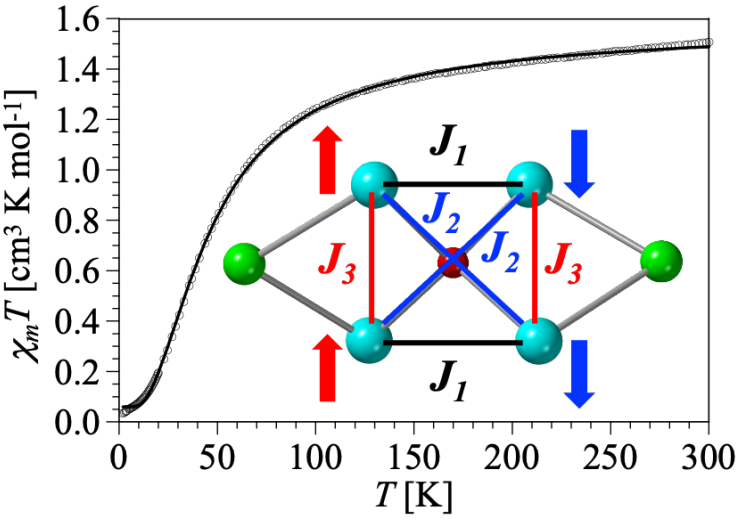

Figure S24. Thermal variation of the product of the magnetic susceptibility per Cu_4 cluster times the temperature ($\chi_m T$) for compound **3**. Solid line is the best fit to a S = ½ tetrahedral tetrameric model.

Table S11. Magnetic parameters obtained from the fits of the magnetic data for compounds **2**, **3**, **5-HCl** and **6-For**.

#	g	J_1 (cm^{-1})	J_2 (cm^{-1})	J_3 (cm^{-1})	zj (cm^{-1})[a]	c (%)[b]	θ (cm^{-1})[c]
2	2.0786(2)	-0.93(1)	-	-	-	-	-
3	2.201(3)	-13.1(1)	-4.5(3)	5.5(5)	-	4.0(3)	-
5-HCl	2.217(1)	-11.4(1)	-	-	-1.03(9)	-	-
6-For	2.089(1)	-	-	-	-	-	-1.42(1)[c]

a) interdimer interaction; b) monomeric paramagnetic impurity; c) Weiss constant.

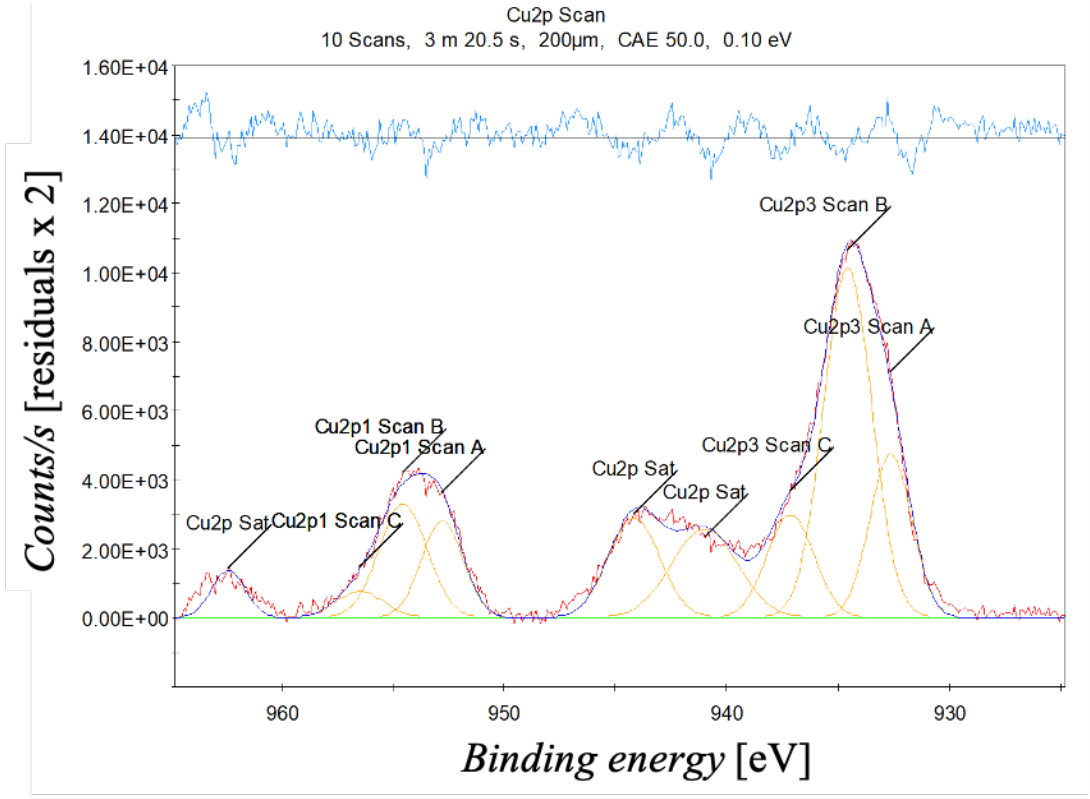

Figure S25. XPS spectrum of MOF **3**.

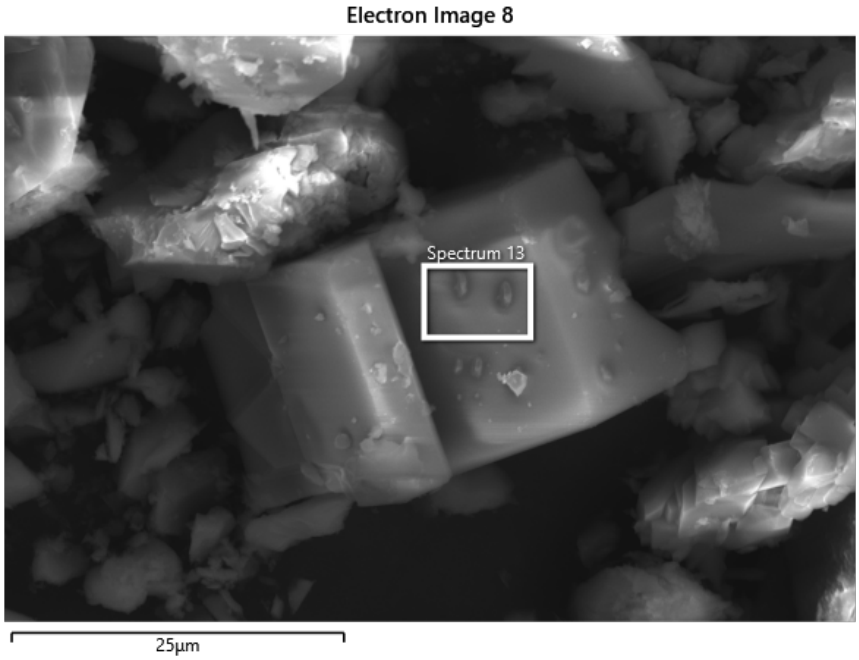

Figure S26. Electron microscopy image of a polycrystalline sample of MOF **3** showing the region for the Energy Dispersive X-ray spectrum.

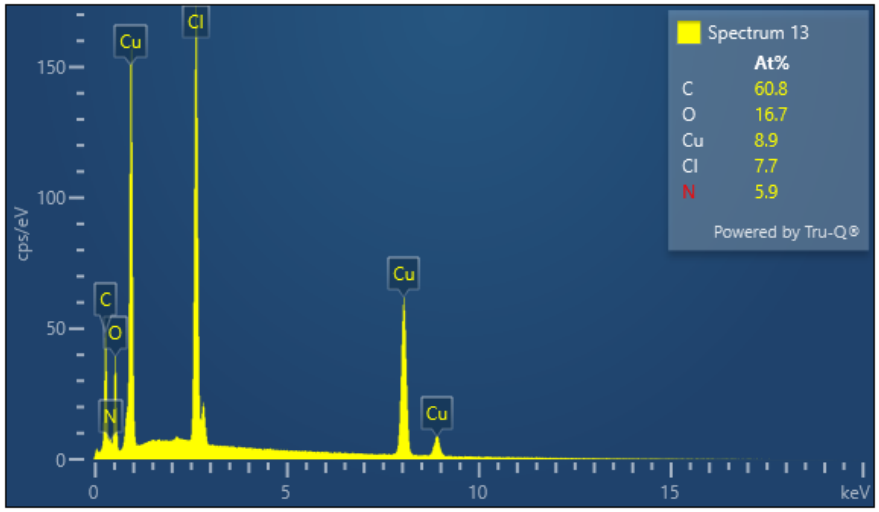

Figure S27. Energy Dispersive X-ray Spectroscopy analysis of the region shown in Figure S26 for MOF **3**.

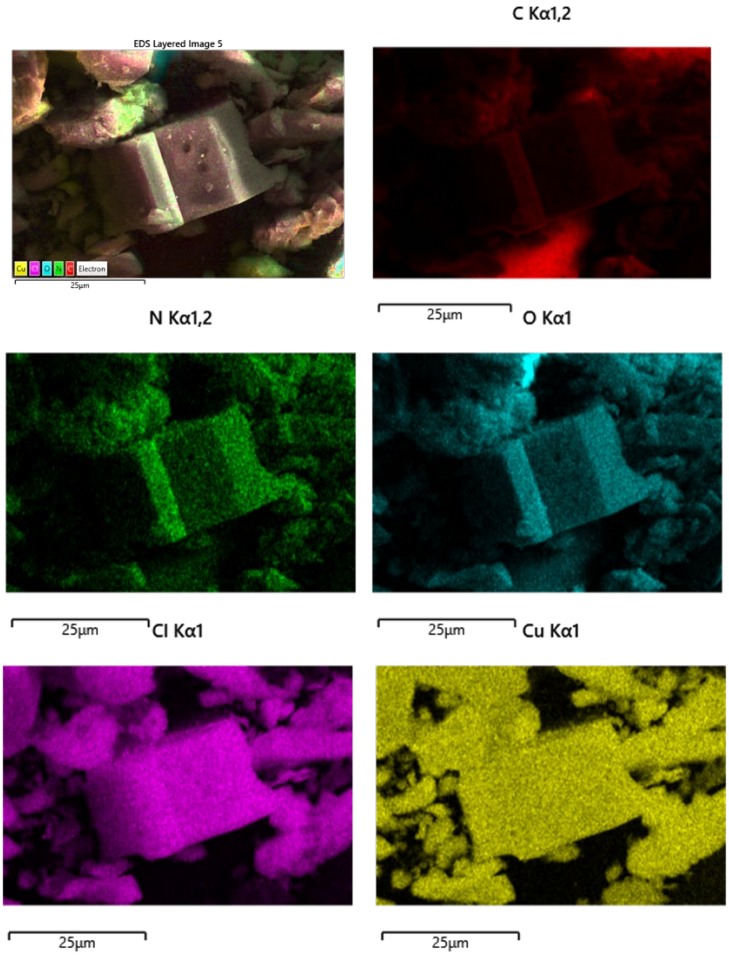

Figure S28. Energy Dispersive X-ray Spectroscopy elemental mapping of MOF **3**.

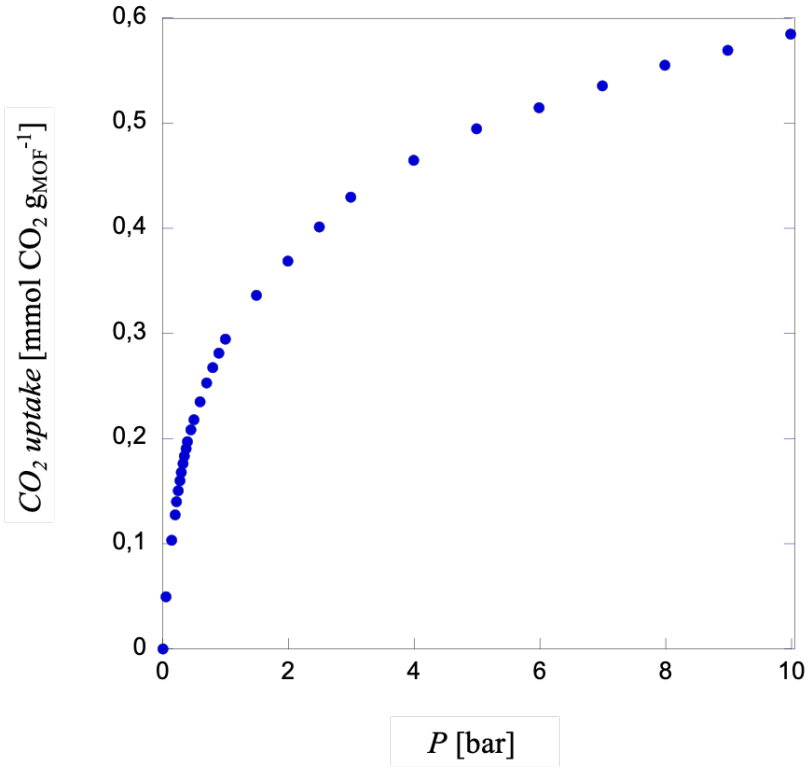

Figure S29. CO_2 sorption isotherm of compound **3** at 273 K.

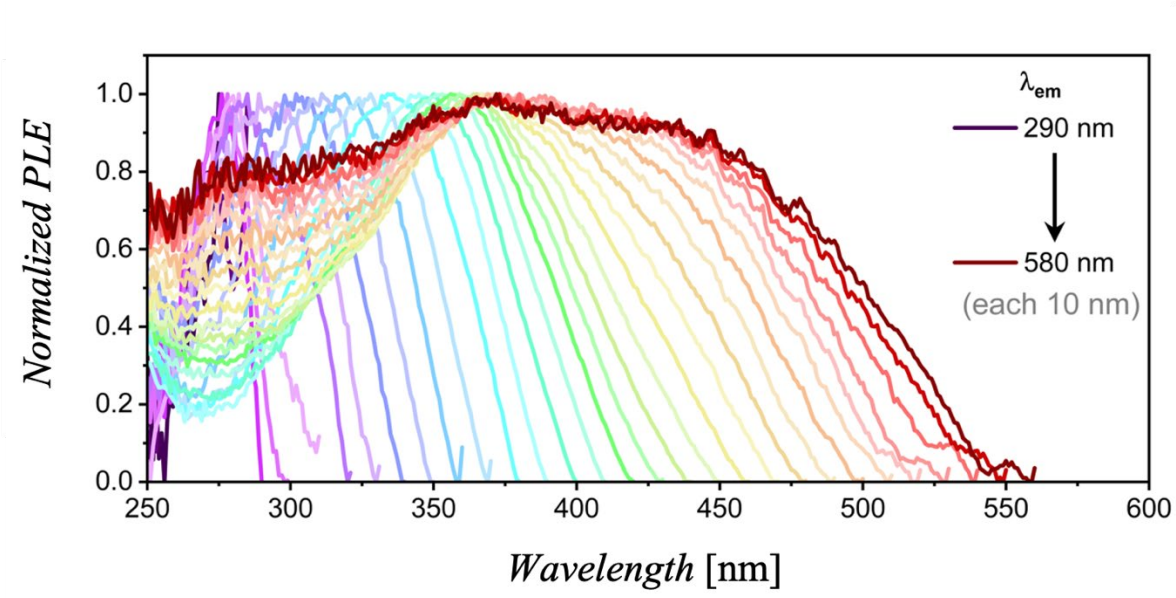

Figure S30. Normalized photoluminescence excitation (PLE) spectra of MOF **3** under different wavelengths.

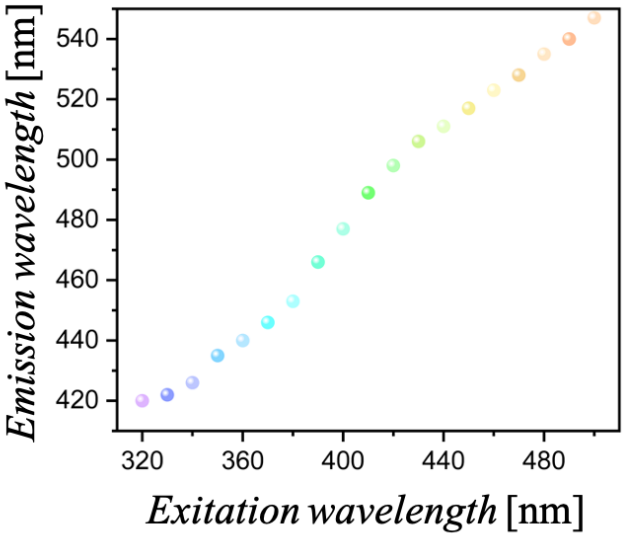

Figure S31. Correlation of the emission wavelength as a function of the excitation wavelength.

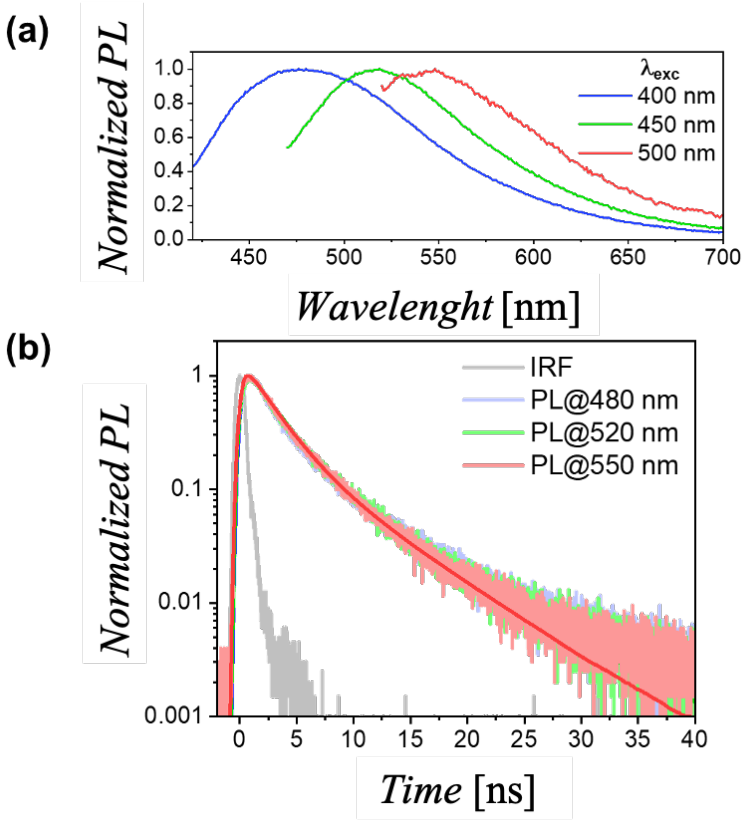

Figure S32. (**a**) Selected PL spectra at different excitation wavelengths. (**b**) Normalized PL

Computational details on the electronic structure calculations of MOF 3

All the theoretical calculations were performed by means of the all-electron, full-potential FHI-aims electronic structure code.[9] The initial structure of MOF **3** was obtained from the experimental data. The unit cell contains two metallic clusters formed by four copper atoms, one central oxo anion and two chloride bridges, coordinated to eight isonicotinate units. Additionally, two dichlorurocuprate(I) guest anions are present, exhibiting a linear geometry and oriented along the direction-*c* pore channels. To compensate the charge of the $CuCl_2^-$ anions, two dimethylammonium ($Me_2NH_2^+$) cations are introduced in the pore channels present along the *a* direction. In order to shed light on the effect of the $CuCl_2^-$ and $Me_2NH_2^+$ guest ions in the structural and electronic properties of MOF **3**, the pristine neutral framework of **3** and the framework plus $CuCl_2^-$ anions (net charge of -2) were also modelled. First, the minimum-energy crystal of the three systems was obtained using the hybrid-DFT HSE06 functional[10] with the tight settings of the tier-1 numerical atom-centered orbital (NAO) basis set, as implemented in FHI-aims. Full ionic and unit cell parameters were relaxed along the geometry optimization through spin-polarized calculations. The initial spin moment was set to 1 for each Cu^{2+} atom of the framework. Single-point calculations were performed on the minimum-energy crystal structures at the same level (HSE06/tier-1 NAO with tight settings) to obtain the electronic band structure and the density of states. A *k*-grid of 3×3×3 was used in all the calculations to explore the reciprocal space along the high-symmetry points of the orthorhombic crystal system. Relativistic effects were considered by using the scalar atomic zero-order regular approximation (ZORA). MOF **3** was also modelled upon one-electron reduction as previously described for the other systems, but with a net charge of -1. Frontier crystal orbitals corresponding to the valence and conduction bands were plotted by means of VESTA software.[11]

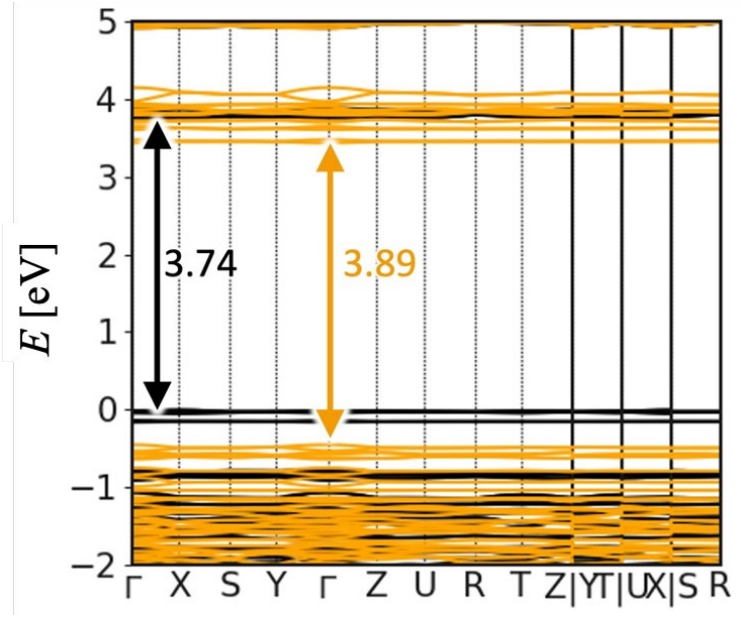

Figure S33. Electronic band structure of the framework of **3** calculated at the HSE06 level of theory. The Fermi level is set to zero at the valence band maximum. α (black) and β (orange) channels are displayed.

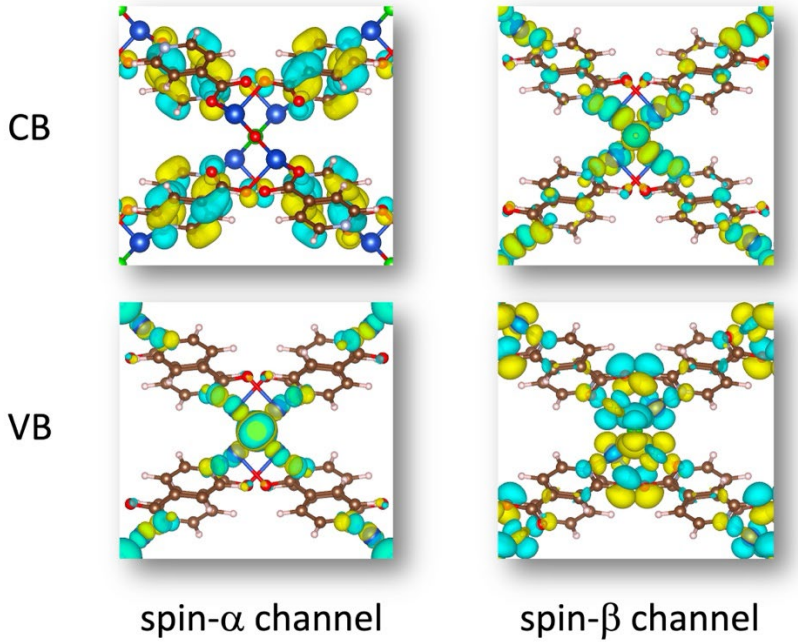

Figure S34. Frontier crystal orbitals of the framework of **3** calculated at the HSE06 level of theory. VB and CB denote valence and conduction bands, respectively.

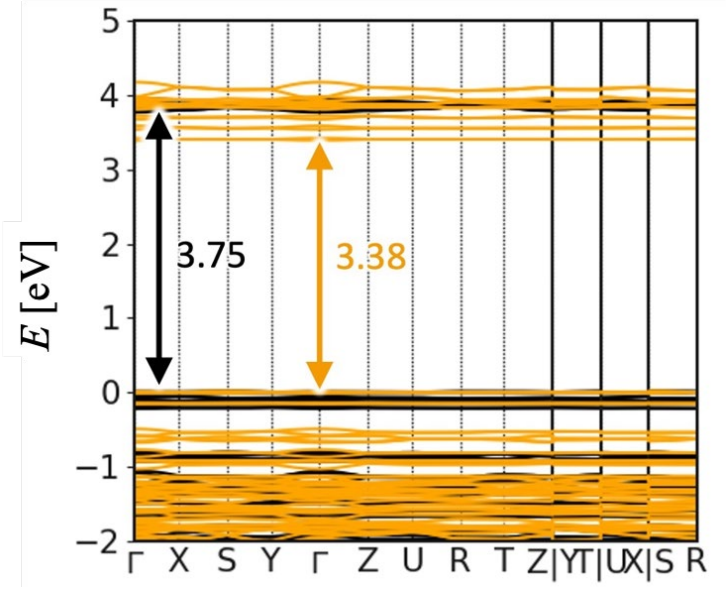

Figure S35. Electronic band structure of the framework of **3** + $CuCl_2^-$ calculated at the HSE06 level of theory. The Fermi level is set to zero at the valence band maximum. α (black) and β (orange) channels are displayed.

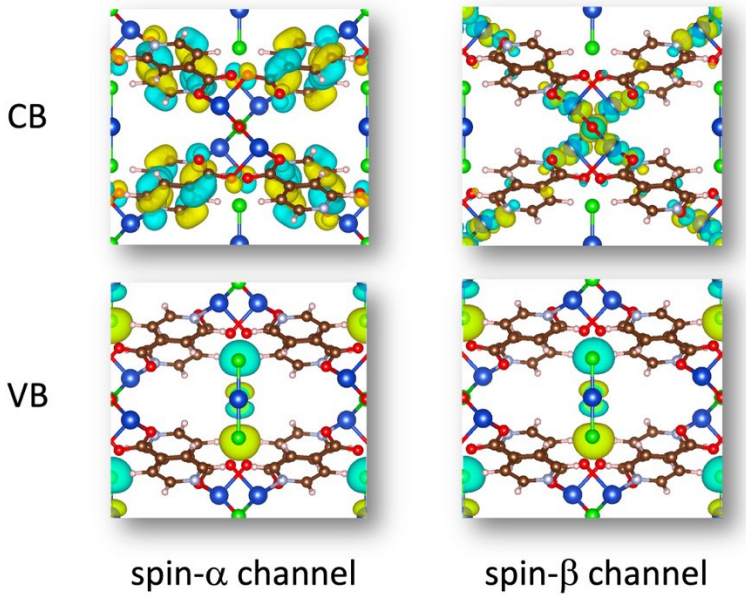

Figure S36. Frontier crystal orbitals of the framework of **3** + $CuCl_2^-$ calculated at the HSE06 level of theory. VB and CB denote valence and conduction bands, respectively.

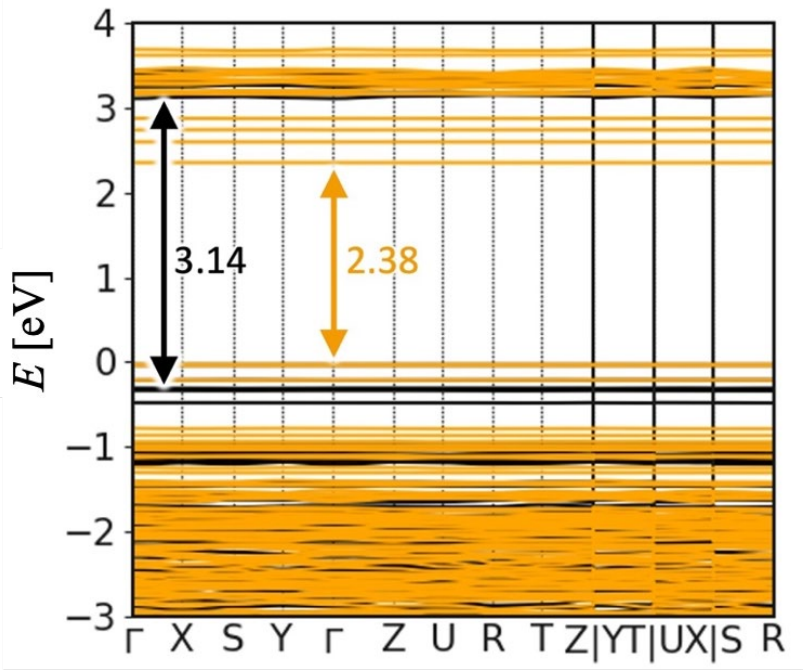

Figure S37. Electronic band structure of **3** (framework + $CuCl_2^-$ + $Me_2NH_2^+$) calculated at the HSE06 level of theory. The Fermi level is set to zero at the valence band maximum. α (black) and β (orange) channels are displayed.

Table S12. Lattice parameters (distances in Å, angles in degrees and volume in $Å^3$) of the unit cell for the PBEsol-optimized crystal structure of the different systems studied.

System	*a*	*B*	*c*	*α*	*β*	*γ*	V
Framework of **3** (F)	13.65	12.41	12.84	90.0	90.0	90.0	2175
F + $CuCl_2^-$	13.71	12.47	12.57	90.0	90.0	90.0	2149
3 (F + $CuCl_2^-$ + $Me_2NH_2^+$)	13.92	13.11	11.26	90.0	90.0	90.0	2055
3 upon one-e^- reduction	13.98	13.16	11.20	89.9	89.8	90.0	2061
3 (experimental)	13.98	12.91	11.64	90.0	90.0	90.0	2101

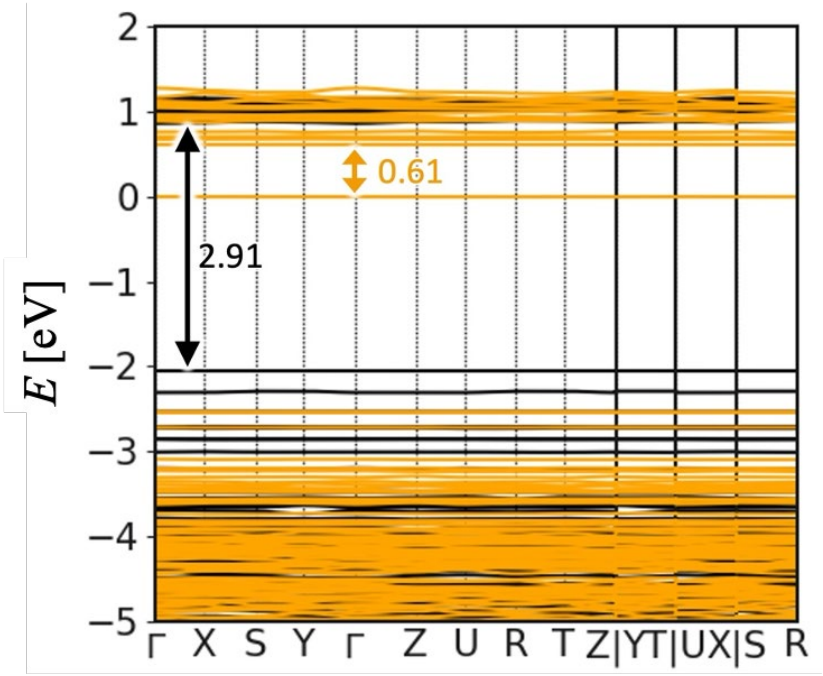

Figure S38. Electronic band structure of **3** (framework + $CuCl_2^-$ + $Me_2NH_2^+$) upon one-electron reduction calculated at the HSE06 level of theory. The Fermi level is set to zero at the valence band maximum. α (black) and β (orange) channels are displayed.

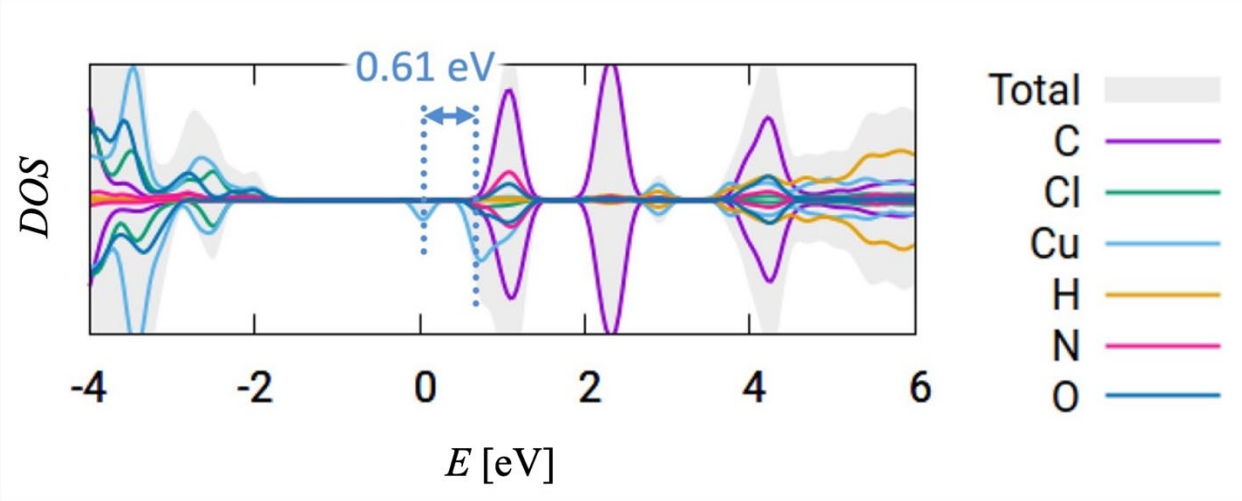

Figure S39. Species-projected density of states of **3** upon one-electron reduction calculated at the HSE06 level of theory.

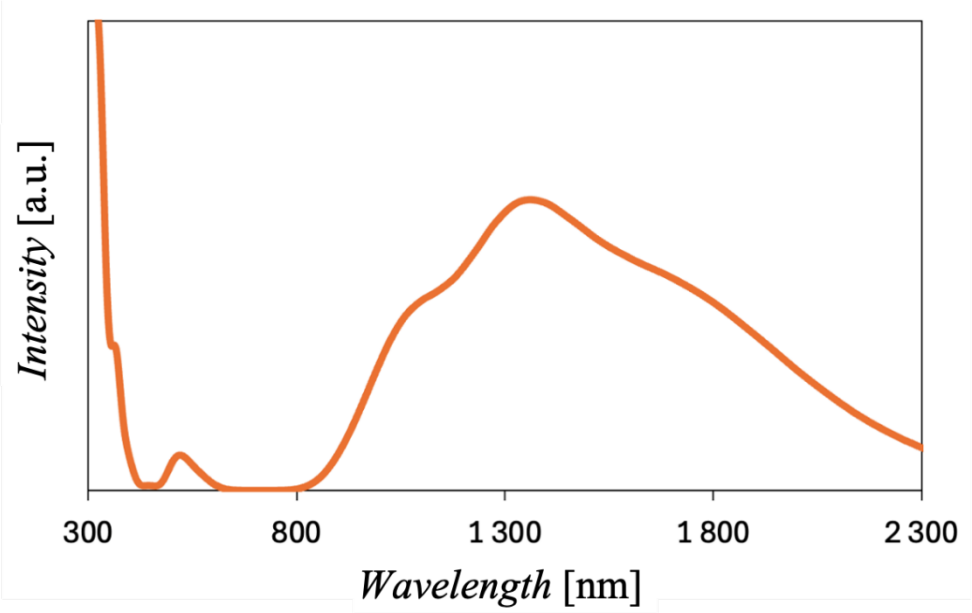

Figure S40. Simulated absorption spectra of MOF **3** upon one-electron reduction.

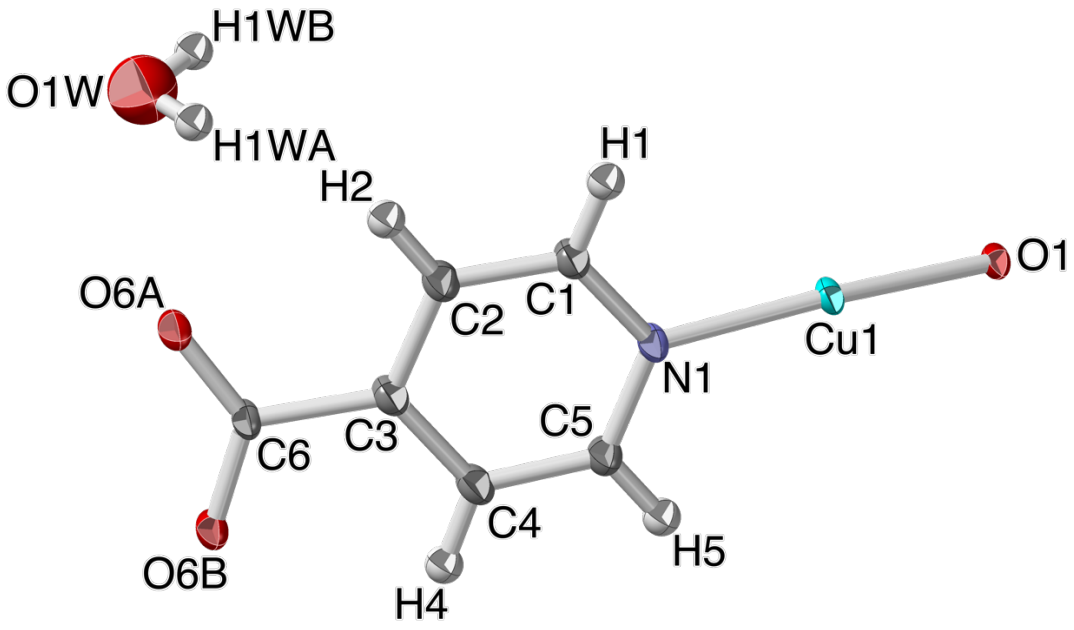

Figure S41. ORTEP plot of the asymmetric unit with labelling scheme of compound [Cu(INA)(OH)]·H_2O (**4-NH_3**). Ellipsoids drawn at 50 % probability.

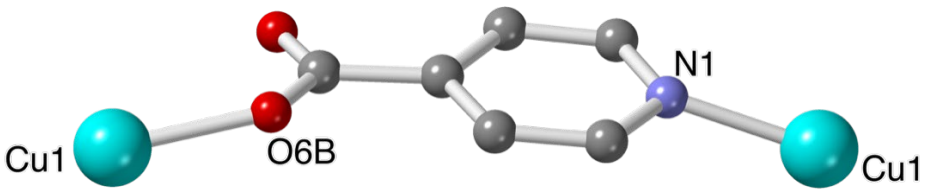

Figure S42. View of one INA^- ligand bridging two Cu^{II} ions through the N1 and O6B atoms in compound $[Cu(INA)(OH)]\cdot H_2O$ (**4-NH$_3$**). Color code: Cu = light blue, C = grey, O = red, and N = dark blue.

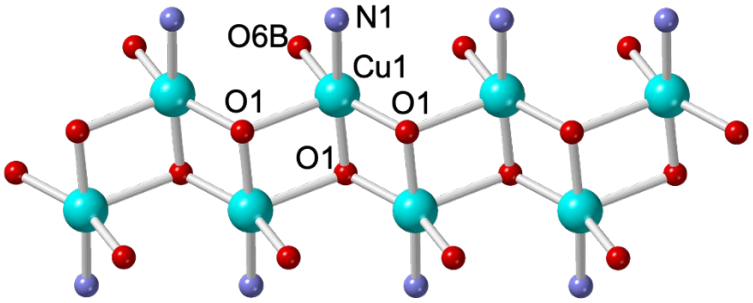

Figure S43. Detailed view of one $[Cu(OH)]_n^{n-}$ chain showing the coordination geometry around the Cu^{II} ions in compound $[Cu(INA)(OH)]\cdot H_2O$ (**4-NH$_3$**). Color code: Cu = light blue, O = red, and N = dark blue.

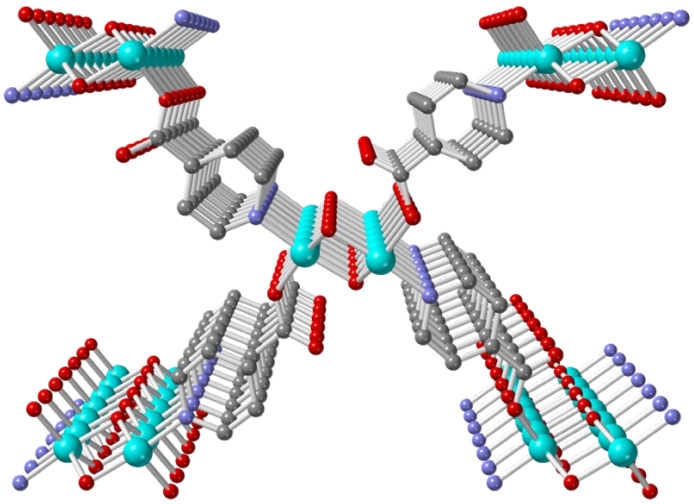

Figure S44. Perspective view along the *a* direction of one $[Cu(OH)]_n^{n-}$ chain connected to four other chains through INA^- bridges in compound $[Cu(INA)(OH)]\cdot H_2O$ (**4-NH$_3$**). Color code: Cu = light blue, C = grey, O = red, and N = dark blue.

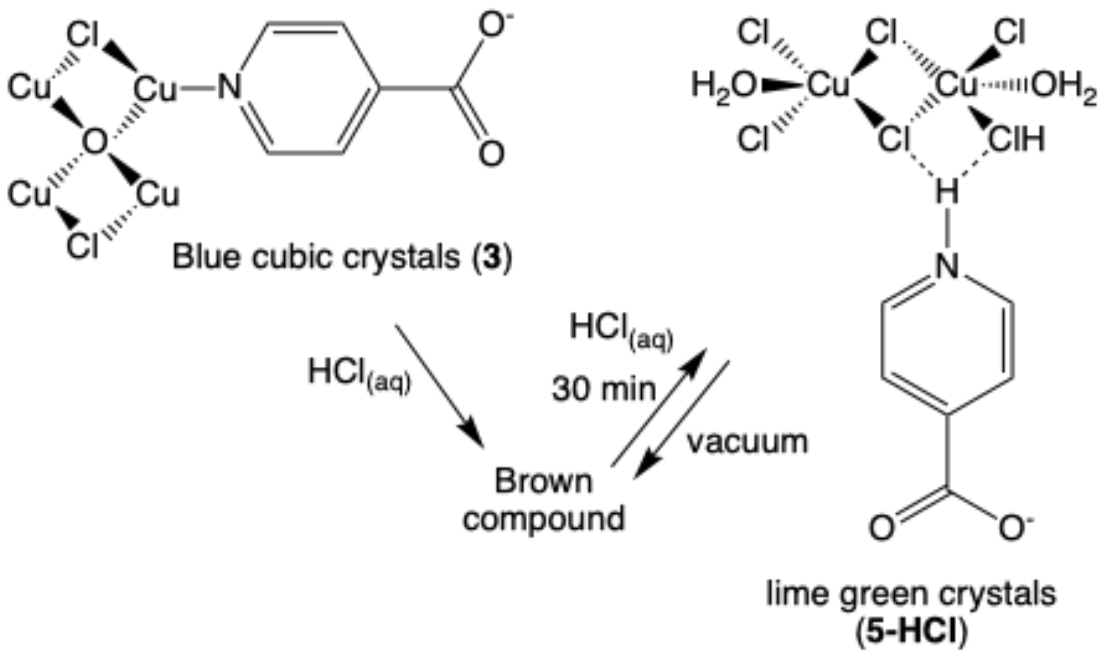

Scheme S1. Probable mechanism of the structural transformation of MOF **3** in presence of HCl vapor to produce **5-HCl** via a brown-colored intermediate.

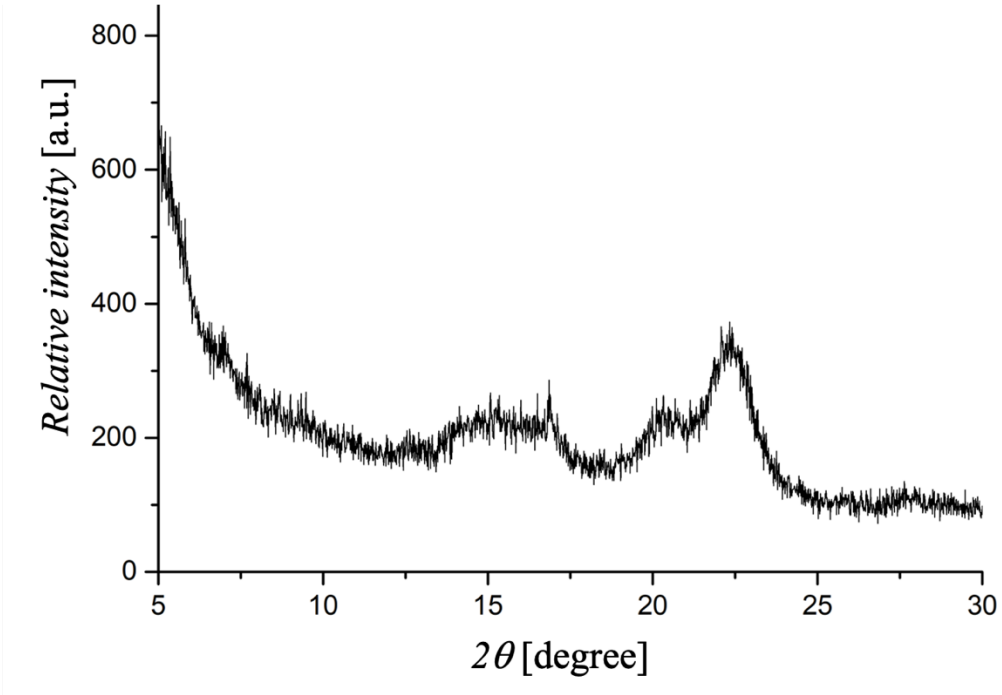

Figure S45. PXRD pattern of the intermediate brown phase obtained from MOF **3** upon exposure to HCl vapor, showing the low crystallinity of this compound.

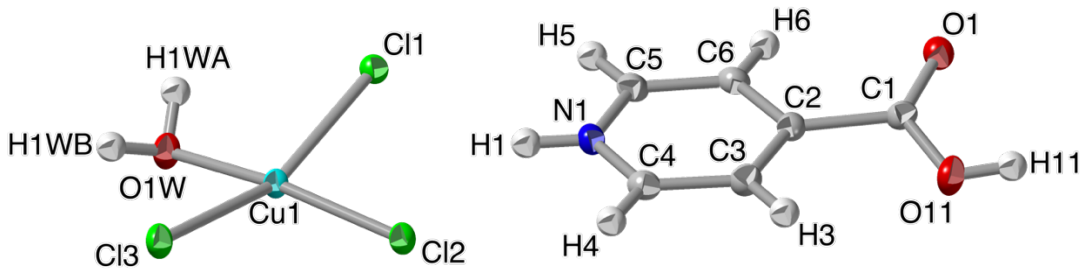

Figure S46. ORTEP plot of the asymmetric unit with labelling scheme of compound $(H_2INA)_2[Cu_2Cl_6(H_2O)_2]$ (**5-HCl**). Ellipsoids drawn at 50 % probability.

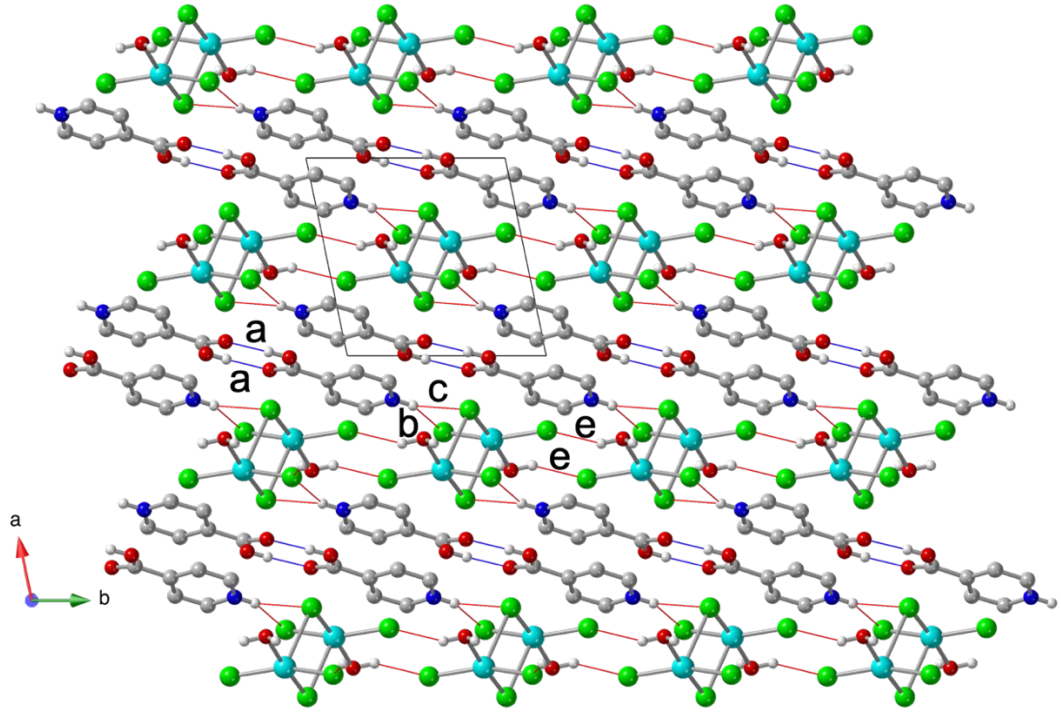

Figure S47. Structure of **5-HCl** in the *ab* plane showing the N-H···Cl bonds (thin red lines) and O-H···O hydrogen bonds (thin blue lines). Labels a-c and e refer to the type of H-bond in Table S13. Color code: Cu = light blue, Cl = green, C = grey, O = red, N = dark blue, and H = white.

Table S13. H-bond parameters in compound **5-HCl**.

Type	D-H···A	D-H (Å)	H···A (Å)	D···A (Å)	<D-H···A> (º)
a	O11-H11···O1	0.840	1.783	2.621	175.8
b	N1-H1···Cl1	0.880	2.561	3.279	139.3
c	N1-H1···Cl2	0.880	2.404	3.115	138.1
d	O1W-H1WA···Cl1	0.870	2.333	3.132	152.8
e	O1W-H1WB···Cl3	0.870	2.396	3.181	150.3

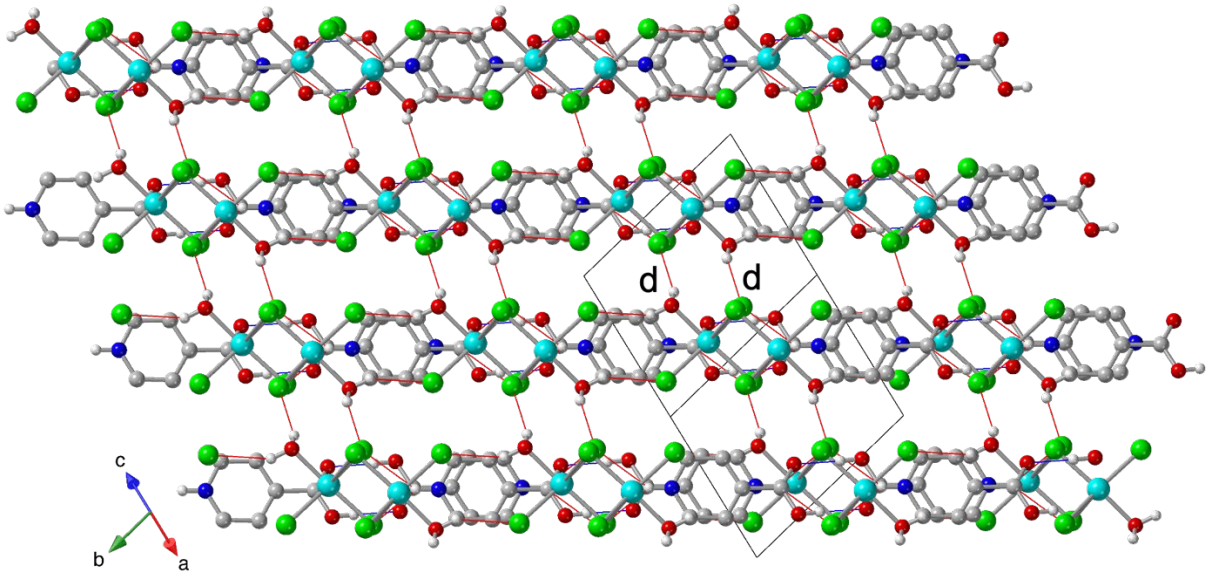

Figure S48. Structure of **5-HCl** along the [101] direction showing the interlayer N-H···Cl bonds (thin red lines). Label d refers to the type of H-bond in Table S13. Color code: Cu = light blue, Cl = green, C = grey, O = red, N = dark blue, and H = white.

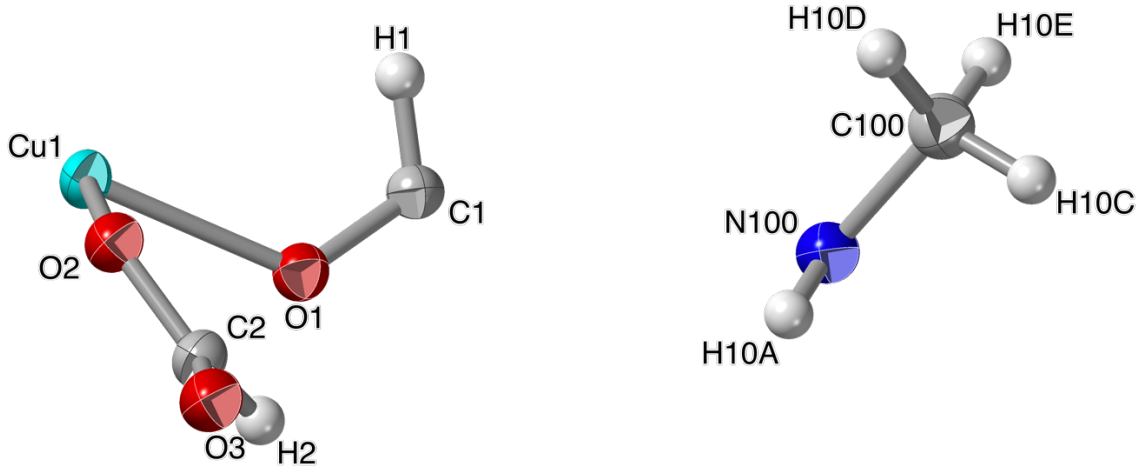

Figure S49. ORTEP plot of the asymmetric unit with labelling scheme of compound $(Me_2NH_2)[Cu(HCOO)_3]$ (**6-For**). Ellipsoids drawn at 50 % probability.

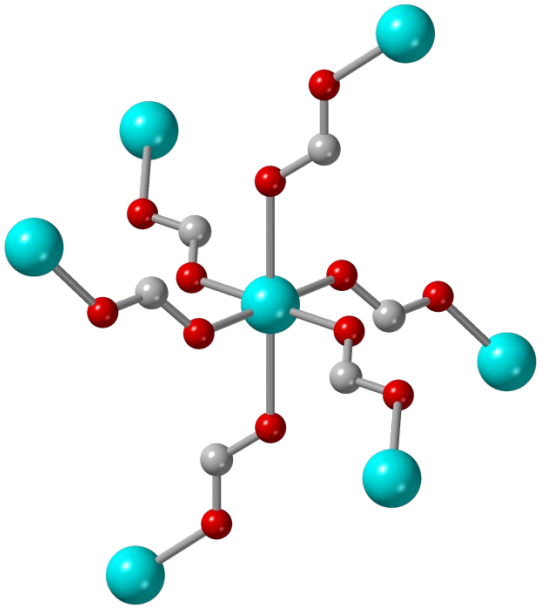

Figure S50. View of one Cu^{II} center surrounded by six other Cu^{II} centers connected through six formate bridges in compound $(Me_2NH_2)[Cu(HCOO)]$ (**6-For**). Color code: Cu = light blue, C = grey, and O = red.

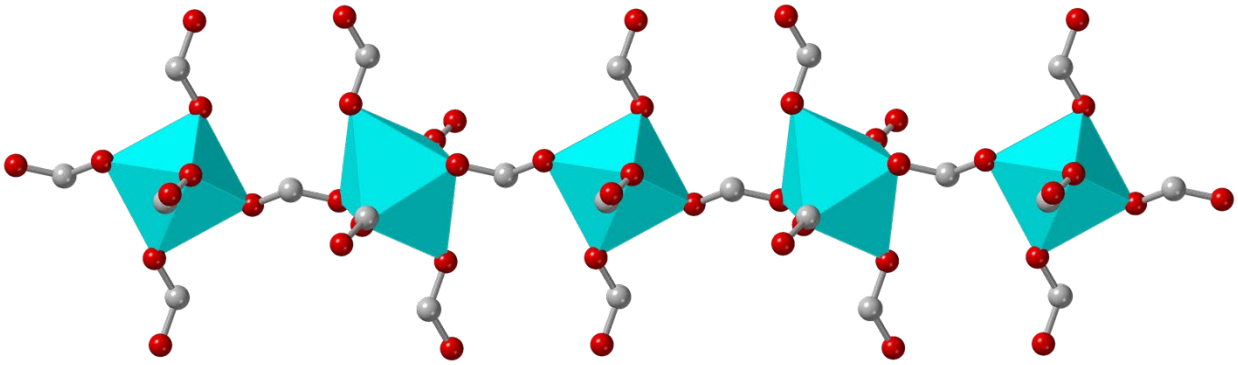

Figure S51. View of one anionic $[Cu(HCOO)]_n^{n-}$ chain showing the elongated octahedral CuO_6 coordination geometry of the Cu^{II} centers and the orientation of their equatorial planes in compound $(Me_2NH_2)[Cu(HCOO)]$ (**6-For**). Color code: Cu = light blue, C = grey, and O = red.

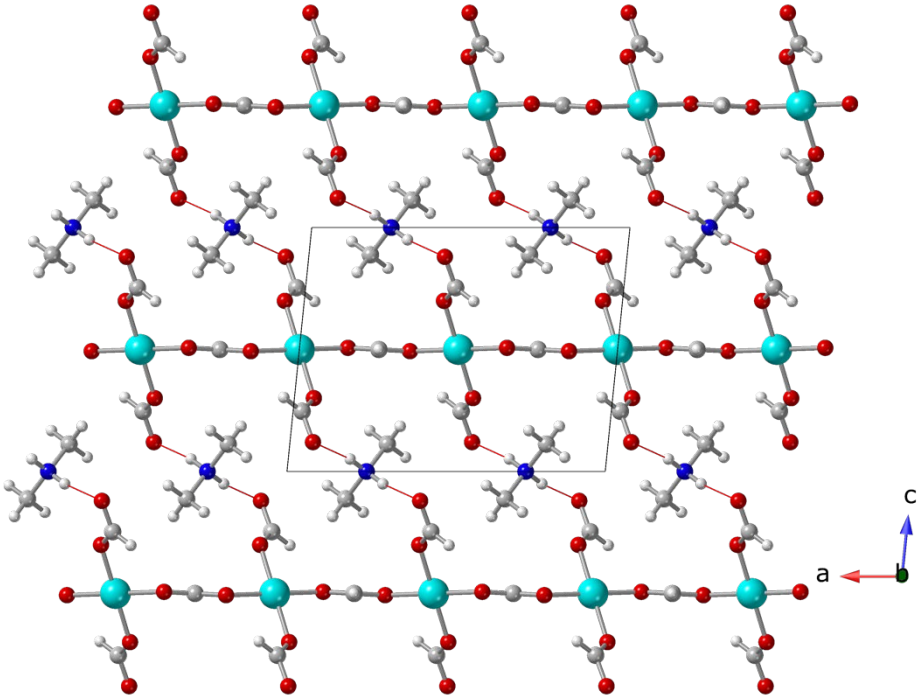

Figure S52. Structure of **6-For** in the *ac* plane showing the N-H···O hydrogen bonds (thin red lines) connecting the $Me_2NH_2^+$ cations and the anionic $[Cu(HCOO)]_n^{n-}$ chains. Color code: Cu = light blue, C = grey, O = red, N = dark blue and H = white.

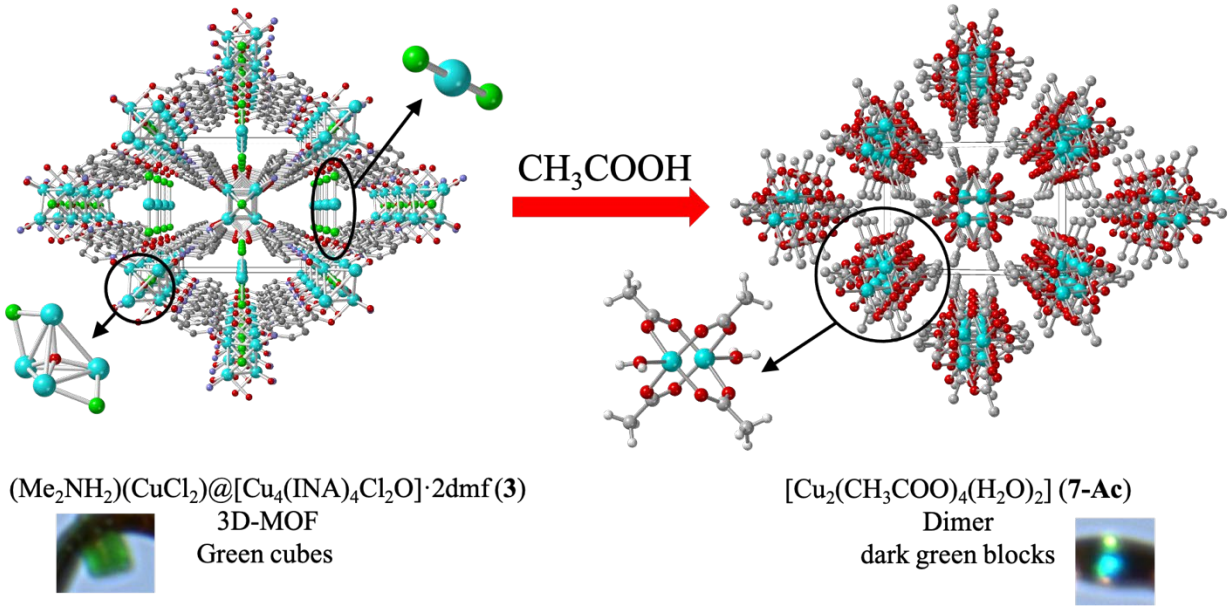

Figure S53. DRST of the 3D MOF **3** into the dimeric compound **7-Ac**. Color code: Cu = light blue, Cl = green, C = grey, O = red, N = dark blue, and H = white.

Magnetic Properties of 5-HCl and 6-For

The thermal variation of the $\chi_m T$ product per Cu^{2+} dimer for compound **5-HCl** shows a room temperature value of around 0.8 cm^3 K mol^{-1}, close to the expected value for two isolated S = ½ Cu^{2+} ions with *g* close to 2. When the temperature is decreased, $\chi_m T$ shows a progressive decrease to reach a value of around 0.07 cm^3 K mol^{-1} at 2 K (Figure S54). This behavior indicates the presence of a predominant antiferromagnetic coupling between the Cu^{2+} ions connected through the double chloride bridge in the Cu_2Cl_6 dimer. Accordingly, we have fitted the magnetic data of **5-HCl** to a Bleaney and Bowers S = ½ dimer model[7] with the parameters listed in **Table S11**. In this case, we need to include a weak interdimer interaction using the mean field approximation to reproduce the magnetic data in the whole temperature range.

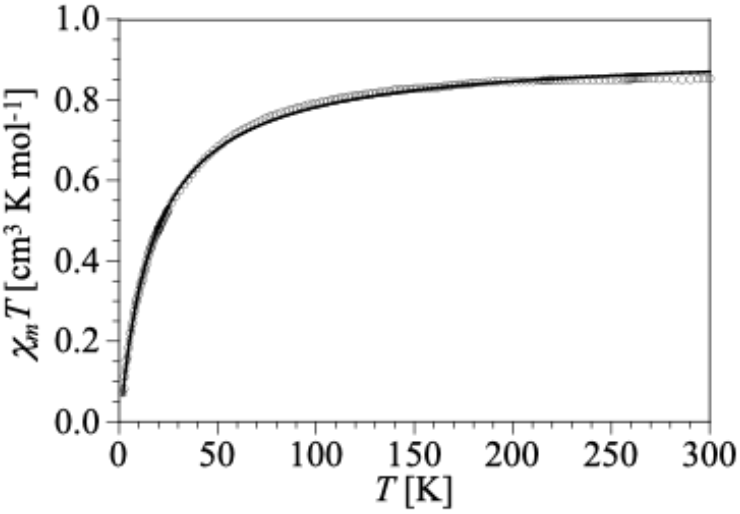

Figure S54. Thermal variation of the product of the magnetic susceptibility per Cu dimer times the temperature (χ_mT) for compound **5-HCl**. Solid line is the best fit to a S = ½ dimer model.

Finally, the thermal variation of the $\chi_m T$ product per Cu^{2+} ion for compound **6-For** shows a room temperature value of around 0.4 cm^3 K mol^{-1}, close to the expected value for one isolated S = ½ Cu^{2+} ions with *g* close to 2. When the temperature is decreased, $\chi_m T$ remains constant down to around 30 K and at lower temperatures it shows a progressive decrease to reach a value of around 0.23 cm^3 K mol^{-1} at 2 K (Figure S55, SI). This behavior indicates the presence of a predominant antiferromagnetic coupling between the Cu^{2+} ions connected through the single *anti-anti* formate bridges. Since the structure of **6-For** shows that each Cu^{II} center is connected to six other through six similar *anti-anti* formate bridges along three orthogonal directions, we have fit

the magnetic data to a simple Curie-Weiss law ($\chi_m^{-1} = C / (T-\theta)$, solid line in Figure S55, SI), with the parameters shown in **Table S11**.

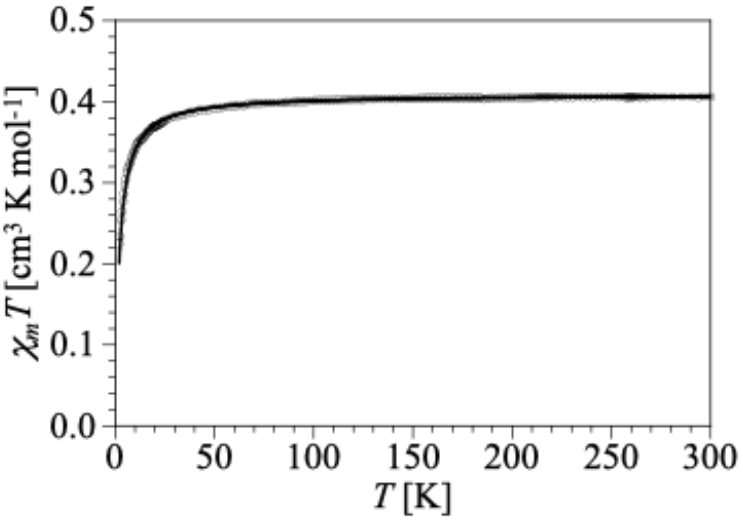

Figure S55. Thermal variation of the $\chi_m T$ product per Cu ion times the temperature for compound **6-For**. Solid line is the best fit to the Curie-Weiss law.

Table S14. Comparison of unit cell dimension of the optimized and X-ray crystal structures.

Compound	Unit cell dimension of optimized structure	Unit cell dimension of experimental X-ray crystal structure
2	*a*: 13.1568, *b*: 8.56074, *c*: 13.8567 α: 90, β: 117.081, γ: 90	*a*: 11.5668(3), *b*: 12.2904(2), *c*: 12.3226(4) α: 90, β: 117.770(4), γ: 90
3	*a*: 14.0054, *b*; 13.2777, *c*: 11.4533 α: 90.4058, β: 90.0338, γ: 90.1942	*a*: 13.9827(3), *b*: 12.9083(4), *c*: 11.6404(4) α: 90, β: 90, γ: 90
4-NH$_3$	*a*: 3.68753, *b*: 16.2734, *c*: 12.6073 α: 90.0265, β: 97.8021, γ: 90.1528	*a*: 3.5276(2), *b*: 15.7899(8), *c*: 12.9885(7) α: 90, β: 96.733(5), γ: 90
5-HCl	*a*: 8.15289, *b*: 8.50989, *c*: 8.63515 α: 115.251, β: 99.7711, γ: 95.2987	*a*: 7.94410(10), *b*: 8.6447(2), *c*: 8.6798(2) α: 116.447(2), β: 98.670(2), γ: 96.527(2)
6-For	*a*: 11.421, *b*: 8.77458, *c*: 8.89063 α: 90.0001, β: 94.3956, γ: 90.0014	*a*: 11.3902(11), *b*: 8.6593(11), *c*: 8.7845(9) α: 90, β: 95.785(10), γ: 90
7-Ac	*a*: 13.0762, *b*: 8.52204, *c*: 13.7188 α: 90.0352, β: 115.982, γ: 89.9886	*a*: 13.0834(1), *b*: 8.5028(1), *c*: 13.7315(1) α: 90, β: 116.865(1), γ: 90[a]

[a] Data taken from reference [12].

References

1. , R. O. D. CrysAlisPro Software System. **2015**.

2. Sheldrick, G. M. SHELXT–Integrated space-group and crystal-structure determination. *Acta Cryst. A* **2015***, 71*, 3–8.

3. Dolomanov, O. V.; Bourhis, L. J.; Gildea, R. J.; Howard, J. A. K.; Puschmann, H. OLEX2: a complete structure solution, refinement and analysis program. *J. Appl. Cryst.* **2009***, 42*, 339–341.

4. Bain, G. A.; Berry, J. F. Diamagnetic corrections and Pascal's constants. *J. Chem. Educ.* **2008***, 85*, 532–536.

5. Saha, R.; Sharma, A.; Siddiqui, A. I.; Benmansour, S.; Ortega-Castro, J.; Frontera, A.; Mondal, B.; Lah, M. S.; García, C. J. G. Simultaneous electron and proton conduction in a stable metal organic material with highly selective electrocatalytic oxygen reduction reaction to water. *Chem. Sci.* **2025***, 16*, 9501–9508.

6. Van Niekerk, J. N.; Schoening, F. A new type of copper complex as found in the crystal structure of cupric acetate, $Cu_2(CH_3COO)_4 \cdot 2H_2O$. *Acta Cryst.* **1953***, 6*, 227–232.

7. Bleaney, B.; Bowers, K. D. Anomalous Paramagnetism of Copper Acetate. *Proc. R. Soc. Lond. A.* **1952***, 214*, 451–465.

8. Chilton, N. F.; Anderson, R. P.; Turner, L. D.; Soncini, A.; Murray, K. S. PHI: A powerful new program for the analysis of anisotropic monomeric and exchange-coupled polynuclear d- and f-block complexes. *J. Comput. Chem.* **2013***, 34*, 1164–1175.

9. Blum, V.; Gehrke, R.; Hanke, F.; Havu, P.; Havu, V.; Ren, X.; Reuter, K.; Scheffler, M. Ab initio molecular simulations with numeric atom-centered orbitals. *Comput. Phys. Commun.* **2009***, 180*, 2175–2196.

10. Krukau, A. V.; Vydrov, O. A.; Izmaylov, A. F.; Scuseria, G. E. Influence of the exchange screening parameter on the performance of screened hybrid functionals. *J. Chem. Phys.* **2006***, 125*.

11. Momma, K.; Izumi, F. VESTA 3 for three-dimensional visualization of crystal, volumetric and morphology data. *J. Appl. Crystallogr.* **2011***, 44*, 1272–1276.

12. Bertolotti, F.; Forni, A.; Gervasio, G.; Marabello, D.; Diana, E. Experimental and theoretical charge density of hydrated cupric acetate. *Polyhedron* **2012***, 42*, 118–127.